Organic aerosol source apportionment by using rolling positive matrix factorization: Application to a Mediterranean coastal city

Benjamin Chazeau, Imad El Haddad, Francesco Canonaco, Brice Temime-Roussel, Barbara d'Anna, Grégory Gille, Boualem Mesbah, André Prévôt, Henri Wortham, Nicolas Marchand

ATMOSPHERIC ENVIRONMENT: X 14 (2022) 100176

Contents lists available at ScienceDirect

Atmospheric Environment: X

journal homepage: www.journals.elsevier.com/atmospheric-environment-x

Organic aerosol source apportionment by using rolling positive matrix factorization: Application to a Mediterranean coastal city

Benjamin Chazeau [a,b,*], Imad El Haddad [c], Francesco Canonaco [c,d], Brice Temime-Roussel [a], Barbara D'Anna [a], Grégory Gille [b], Boualem Mesbah [b], André S.H. Prévôt [c], Henri Wortham [a], Nicolas Marchand [a,**]

[a] Aix Marseille Univ, CNRS, LCE, Marseille, France
[b] AtmoSud, Regional Network for Air Quality Monitoring of Provence-Alpes-Côte-d'Azur, Marseille, France
[c] Laboratory of Atmospheric Chemistry, Paul Scherrer Institute (PSI), 5232, Villigen-PSI, Switzerland
[d] Datalystica Ltd., Park InnovAARE, 5234, Villigen, Switzerland

A B S T R A C T

We investigated the contributions and the evolution of organic aerosol (OA) sources at the Marseille-Longchamp supersite (MRS-LCP, France) based on Time-of-flight Aerosol Chemical Speciation Monitor (ToF-ACSM) measurements of non-refractory PM_1 over a fourteen-month period (1 February – 3 April 2018). The OA source apportionment was performed by positive matrix factorization (PMF) using the novel "rolling window" approach implemented in the Source Finder Professional (SoFi Pro). Here, PMF is performed over a 14-days window moving over the entire OA dataset, in order to account for the temporal variability of the source profiles.

Six factors were resolved, including hydrocarbon-like organic aerosol (HOA) which is related to traffic exhausts, cooking-like organic aerosol (COA), biomass burning aerosol (BBOA), less oxidized organic aerosol (LOOA), more oxidized organic aerosol (MOOA) and a new defined source related to the mix between shipping and industrial plumes (Sh-IndOA). While HOA and COA consistently contribute to the total OA with on average 11.2% (ranging between 9.2 and 12.1% over the seasons) and 11.5% (11–12.1%), respectively, BBOA (11.7% on average) shows a larger seasonal variability with 18% in winter and no contribution in summer. BBOA profiles during winter were attributed to fresh biomass burning emissions from domestic heating, and more oxygenated profiles were assigned to regional land and agricultural waste burning for spring and early autumn. Sh-IndOA fraction is estimated to 4.5% (3.7–6.1%) and contributes to the total OA mass concentrations to a minor extent. The secondary organic aerosol (SOA) fraction includes both LOOA with 21.5% (18.8–27.2%) and MOOA with 39.6% (36.8–42.6%). Based on the f44/f43 analysis these sources appeared to be more linked to biogenic influences in summer, whereas the concentrations were associated with oxidized anthropogenic sources (biomass burning and road traffic) for the rest of the year. The investigation of MOOA geographical origins suggests some influence of air masses transported from the Rhône Valley and the west basin of the Mediterranean Sea.

1. Introduction

The exposure to atmospheric particulate matter (PM) causes millions of annual premature deaths worldwide (Cohen et al., 2017; Lelieveld et al., 2015). It is well known that fine particles (PM_1; PM with an aerodynamic diameter smaller than 1 μm) may cause the highest damage to human health (Kreyling et al., 2006; Oberdörster et al., 2004) and trigger respiratory and cardiovascular diseases and lung cancers (Pope et al., 2002; Pope and Dockery, 2006). The health effect might also differ according to the different aerosol sources (Daellenbach et al., 2020).

Organic aerosol (OA) represents the major constituent of the fine PM mass composition (Jimenez et al., 2009) and knowledge about its main sources and formation processes increased considerably over the last decades. This fraction can be classified as primary OA (POA) corresponding to particles directly emitted in the atmosphere, or secondary OA (SOA) which are formed via condensation or uptake of oxidized gas-phase precursors. The aerosol mass spectrometer (AMS) (Canagaratna et al., 2007; Jayne et al., 2000) has been extensively used for the online analyses of the non-refractory submicron aerosol ($NR\text{-}PM_1$) composition. While the studies using AMS are limited to short-term campaigns, the aerosol chemical speciation monitor (ACSM) (Fröhlich et al., 2013; Ng et al., 2011b), based on the same technology, is easily deployed for unattended long-term monitoring (up to multiple years). A great advantage is to allow the investigation of the seasonality and yearly variations of the dataset.

AMS and ACSM are widely deployed worldwide in order to quantify and identify the OA emission sources (Fröhlich et al., 2015a; Zhang et al., 2011). Source apportionment of OA is commonly performed using

* Corresponding author. Aix Marseille Univ, CNRS, LCE, Marseille, France.
** Corresponding author.
E-mail addresses: benjamin.chazeau@univ-amu.fr (B. Chazeau), nicolas.marchand@univ-amu.fr (N. Marchand).

https://doi.org/10.1016/j.aeaoa.2022.100176
Received 4 November 2021; Received in revised form 8 April 2022; Accepted 25 April 2022
Available online 28 April 2022

positive matrix factorization (PMF; Paatero and Tapper, 1994). The PMF algorithm can be solved with the multilinear engine (ME-2; Paatero, 1999) which allows to introduce a-priori information to the factor profiles and/or time series (Canonaco et al., 2013; Crippa et al., 2014; Lanz et al., 2008). In Europe, several studies conducted OA source apportionment over large dataset (>1 year) using AMS (Ovadnevaite et al., 2014; Young et al., 2015), offline-AMS (Bozzetti et al., 2017b; Daellenbach et al., 2016, 2017; Vlachou et al., 2018, 2019) and ACSM (Bressi et al., 2016; Canonaco et al., 2015; Fröhlich et al., 2015b; Heikkinen et al., 2020; Minguillón et al., 2015; Ripoll et al., 2015; Schlag et al., 2016; Stavroulas et al., 2019; Via et al., 2021; Zhang et al., 2019). As factors seasonal variations can't be properly modelled with static profiles generated with a year-long PMF, most of the studies had to apply multi-seasonal PMF over their dataset. However, this method is likely to produce several seasonal factors representations leading to discontinuities between each PMF solutions. To overcome this limitation, a novel approach was developed and consists in applying PMF on a smaller and moving time window (Canonaco et al., 2021; Parworth et al., 2015). This so-called "rolling window" method allows to capture the temporal variability of the factor profiles and results in shorter computational times for each PMF run. and was successfully applied to two sites in Switzerland (Zurich; Canonaco et al., 2021 and Magadino; Chen et al., 2021) and one in Poland (Krakow; Tobler et al., 2021).

This study presents a fourteen-month long dataset measured with a ToF-ACSM in Marseille, a coastal city in the south of France, between February 2017 and April 2018. We conducted a complete PMF analysis on organic aerosol based on the "rolling window" technique. To our knowledge, this is the first study using this novel PMF approach over an up-to-1 year ToF-ACSM dataset. We compare the rolling results to standard seasonal PMF analysis and further, estimate and investigate the BBOA and SOA origins over the study period.

2. Materials ad methods

2.1. Sampling site and instrumentation

Sampling site description and general conditions were detailed elsewhere (Chazeau et al., 2021; El Haddad et al., 2011a, 2013) and will be briefly outlined in this paper. Marseille-Longchamp supersite (MRS-LCP) is located in the downtown park "Longchamp" (43°18′18.84″N; 5°23′40.89″E; 71 m a.s.l.) and hosted for 15 years a monitoring station of the regional association of air quality (AtmoSud, https://www.atmosud.org). This site is representative of urban background pollution over the area of Marseille.

The chemical composition of non-refractory submicron aerosol was measured continuously from February 2017 to April 2018 using the time-of-flight aerosol chemical speciation monitor (ToF-ACSM). A detailed description of the instrument operating principle and analysis procedures are provided by Fröhlich et al. (2013) and Timonen et al. (2016). The NR-PM_1 aerosol is sampled at a flow rate of 3 L min^{-1} and dried using a Nafion dryer system (Perma Pure, New Jersey, USA) which allowed to keep the relative humidity (RH) below 40%. The ToF-ACSM was operated between m/z 12 and 214 and produced averaged scans every 15 min. The data were acquired using Igor-DAQ v.2.1.4 software and by Tofware v.2.5.13 written in Igor Pro (Wave Metric inc., Lake Oswego, Oregon, USA).

Necessary calibrations and data corrections are detailed in Chazeau et al. (2021). Calibrations of ionization efficiency (IE) of nitrate and relative ionization efficiency (RIE) of ammonium and sulfate were performed three times over the 2017–2018 period, and blank measurements were achieved one time for determining detection limits of ToF-ACSM species. The collection efficiency (CE) values were corrected using algorithms described by Middlebrook et al. (2012) and an averaged value of 0.47 was used for this dataset. According to Pieber et al. (2016) ammonium nitrate can contribute to m/z 44 and cause an overestimation of the organic signal. This interference was corrected and showed negligible contribution of NH_4NO_3 on the organic m/z 44 (CO_2^+) with value ranging from 0.1 to 0.5%.

A dual spot Magee Scientific AE-33 Aethalometer (Drinovec et al., 2015) was deployed since 2014 on MRS-LCP site, operating at a 1 min resolution and a 5 L min^{-1} flow rate. The light attenuation was measured at seven wavelengths ranging from the ultraviolet to near infrared (at 370, 470, 520, 590, 660, 880 and 950 nm). The BC concentrations can be deconvolved into two contributions, fossil fuel (BC_{FF}) and wood burning (BC_{WB}) using the aethalometer model (Sandradewi et al., 2008). The 470 and 950 nm wavelengths were used with an Angström exponent of 1.68 and 1.02 for pure wood burning and traffic, respectively, as recommended by Zotter et al. (2017) and Chazeau et al. (2021). Aerosol number size distribution was investigated with the model 3031 ultrafine particle monitor (TSI Inc., Minnesota, USA) providing measurements from 20 to 1000 nm with six channels of size resolution. Furthermore, a Scanning Mobility Particle Sizer system (SMPS, L-DMA, CPC5403, GRIMM) was deployed over two periods: from 23 June to August 12, 2017 (summer period) and from November 6, 2017 to January 11, 2018 (winter period). The particle size distribution was measured in the size range 10.25–1084 nm. In addition, all data including O_3, NO_x, SO_2, PM_1, $PM_{2.5}$ and PM_{10} 15 min-averaged concentrations were also measured with the standard real-time equipment of AtmoSud available directly on site. Finally, temperature, wind directions and speeds were recorded with an anemometer sonic 3D since June 2017. Non-parametric wind regressions (NWR) were performed to estimate the OA source concentrations at given wind direction and speed (Henry et al., 2009). The OA factors were also coupled with 72h-backtrajectories calculated every 6 h from the HYSPLIT model (Stein et al., 2015) using weekly 1° Global Data Assimilation System (GDAS) meteorological field data. Their geographical origin was explored through Concentration-Weighted Trajectory (CWT) (Ashbaugh et al., 1985) which were performed at the MRS-LCP endpoint (43°18′18.84″N; 5°23′40.89″E; 64 m a.g.l.) with a resolution of 0.1° × 0.1° and for the entire study period. To minimize the important dilution affecting air masses in the free troposphere backtrajectories above 1500 m a.g.l. were discarded (Debevec et al., 2017; Michoud et al., 2017). These analyses were conducted with the ZeFir toolkit v.3.7 (Petit et al., 2017b).

2.2. Source apportionment method

Source apportionment was performed on ToF-ACSM OA mass spectra using Positive Matrix Factorization (PMF; Paatero and Tapper, 1994) for the 14 months period in Marseille. PMF algorithm is solved by the multi-linear engine (ME-2; Paatero, 1999) with the software package SoFi (Source Finder; Canonaco et al., 2013) coded in Igor Pro. PMF is a bilinear unmixing model that describes the variability of a multivariate dataset as a linear combination of factor profiles times their time series as described in the following:

$$x_{i,j} = \sum_{k=1}^{p} g_{i,k} \cdot f_{k,j} + e_{i,j} \quad (1)$$

Here, $x_{i,j}$ corresponds to the measurement matrix, $g_{i,k}$ the factor time series, $f_{k,j}$ the factor profiles and $e_{i,j}$ the model residuals. The index i, j, k and p correspond to the time elements, variables (ToF-ACSM OA fragments), factor numbers and total number of factors selected, respectively. ME-2 solver fits the non-negative entries in $g_{i,k}$ and $f_{k,j}$ using a least squares algorithm to iteratively minimize the object function Q (Eq. (2)) defined as the sum of the squared residuals (e_{ij}) weighted by their respective uncertainties (σ_{ij}):

$$Q = \sum_i \sum_j \left(\frac{e_{ij}}{\sigma_{ij}}\right)^2 \quad (2)$$

The error matrix σ_{ij} was calculated by Tofware v.2.5.13 software and includes ion counting statistics (Allan et al., 2004), background errors and electronic noise. A minimum error corresponding to the

measurement of a single ion was also applied to the error matrix. To inspect the object function Q for different PMF runs, Q/Q_{exp} is calculated and defined as Q normalized by the degree of freedom of the model solution (Q_{exp}). Following the recommendations of Paatero and Hopke (2003), a step function is applied for removing variables with signal-to-noise ratio (S/N) less than 0.2 ("bad" variables) and down-weighting those with S/N between 0.2 and 2 ("weak variables"). Here no variable was considered as "bad" (Figure A1) and m/z 208 was down-weighted by a factor of 2 (Ulbrich et al., 2009). Variables calculated based on m/z 44 in the OA fragmentation table (ie. m/z 16, 17, 18 and 28) were automatically excluded for the PMF analysis and reinserted for *post*-PMF analysis.

The PMF input matrix included 185 variables (from m/z 12 to m/z 214) and 16,485 time points (data with a time step of 15 min were re-averaged to 30 min for speeding up computation time). PMF was operated in the robust mode, in which outliers with $\sigma_{ij} \ll e_{ij}$ were down-weighted. A common potential problem in PMF is the solution rotational ambiguity, where several combinations of $f_{k,j}$ and $g_{i,k}$ may result in the same goodness-of-fit. The ME-2 solver enables efficient exploration of the rotational ambiguity and offers high rotational control. Here, the solutions were oriented toward environmentally meaningful rotations by constraining elements of factor profiles ($f_{k,j}$) and factor time series ($g_{i,k}$). Constraints are achieved with known inputs profile/time series and the scalar a defined as the extent to which the outputs $f'_{k,j}/g'_{i,k}$ are allowed to vary during the model iteration:

$$f_{kj} = f'_{kj} \pm a \cdot f'_{kj} \quad (3)$$

$$g_{ik} = g'_{ik} \pm a \cdot g'_{ik} \quad (4)$$

The index j represents the m/z variable and i the measured point in time of the kth factor. The a-value approach is a successfully applied and well documented method for unmixing sources and it removes environmentally unreasonable factors for AMS/ACSM datasets (Canonaco et al., 2013; Lanz et al., 2008).

PMF was performed using a fixed rolling PMF window, which moves over the entire input dataset. Instead of modelling static factor profiles this dynamic PMF allows catching source profiles variability over time. The technique is available in the additional module 'SoFi Pro', recently implemented in the SoFi software package (Canonaco et al., 2021). With this tool the user can easily select the width of the PMF window, the shift and the number of repeats per PMF window adapted to the dataset. Due to the large number of generated PMF runs, a criteria-based panel was built to either automatically accept or reject environmentally reasonable solutions. The results are then explored through several statistical analyses and graphic visualisations available in the current version of the module.

3. Optimization of the OA source apportionment and rolling PMF approach

3.1. Number of factors

The number of factors was first inspected based on residual analysis of unconstrained seasonal runs. These tests were achieved separately for different seasons in order to take into consideration the variability in the source profiles. A range of solutions with 1–10 factors was examined for each season according to the Q/Q_{exp} evolution when increasing the number of factor. The large changes of the Q/Q_{exp} indicate a significant decrease in residuals and an improvement in the explained variability by the model. The $\Delta Q/Q_{exp}$ were calculated as the difference between p factor solutions and the p-1 factor solutions. For winter and autumn the $\Delta Q/Q_{exp}$ largely decreased until six factors and for summer and spring until five factors (Table A1). Solutions with higher number of factors provided small changes in terms of $\Delta Q/Q_{exp}$. The second step was to inspect whether seasonal solutions with the recommended factors combination from residual analysis were environmentally meaningful. Comparison with reference mass spectra, time series of external tracers and diurnal trends were used to relate the factors extracted by PMF to specific sources or processes. A detailed discussion of factors identification is described in the Supplement. For all seasons, 2 primary factors (HOA and COA) and 2 secondary/oxygenated factors (LOOA and MOOA) were identified. The oxygenated OA (OOA) was separated into two different factors as they displayed distinct diurnal variability and different relative contributions from oxygenated ions at m/z 43 and m/z 44 (Figure A2). A BBOA factor was determined during all seasons except summer, which can be easily explained by the absence of domestic heating in summer and a lack of wildfire in the area during summer 2017. The residual did not exhibit strong diurnal structures (Figure A3), which also suggests that the model captures the major sources (Crippa et al., 2014). However, HOA and COA factors were mixed in a single factor in all the seasonal unconstrained solutions and did not have typical diurnal profiles (Figure A4). Unconstrained PMF does not allow a clear separation as their mass spectra profiles are very similar (contributions of alkyl fragments like m/z 43, m/z 55 and m/z 57) and thus the use of constraint from reference mass spectra is required.

In previous studies an industrial related OA factor was resolved at the MRS-LCP station with online and offline AMS datasets (Bozzetti et al., 2017a; El Haddad et al., 2013). This factor was attributed to plumes (associated with high ultrafine particle number and SO_2 concentrations) emitted from the industrial area of Fos-sur-mer located 40 km northwest of the city. As discussed in Chazeau et al. (2021), these plumes are advected by West/South-West sea breeze toward the receptor site and are highly mixed with shipping emissions from the Marseille harbour. In this study, the PMF analysis revealed an influence of this mixed shipping/industrial factor (Sh-IndOA) only with a solution up to 13 factors (Figure A5). As not all the remaining factors in the 13-factor solution could be interpreted, we have selected 5–6 factor solutions where the Sh-IndOA was constrained.

3.2. Rotational ambiguity exploration

Both HOA and COA factor profiles were constrained using the a-value approach, with reference profiles derived from several datasets from Ng et al. (2011a) and Crippa et al. (2013), respectively. The identification of COA is based on its diurnal cycles with maxima at lunch and dinner times. We have considered that the increase in COA concentrations during traffic rush hours to be an indication of the mixing between HOA and COA. We conducted an a-value sensitivity analysis over the whole study period by scanning a-value combinations for HOA and COA with an a-value step size of 0.1 in the range between 0 and 1 leading to 121 possible outcomes (Bozzetti et al., 2017a; Daellenbach et al., 2016; Elser et al., 2016). A-value combinations were retained based on statistical criteria as described in the following. For the set of 121 PMF solutions obtained from the sensitivity analysis, solutions were categorized according to the Pearson correlation coefficient between HOA and COA profiles and reference mass spectra. The main goal was to prove that a profile can unambiguously be ascribed to a specific source and to reject the solution where this is not the case. This was achieved by conducting chi squared tests (χ^2) which investigate if a set of variables (here correlation coefficients) is identical. This test computes the χ^2 value for the correlation coefficients and compares it to the critical value (Eq. (5)) at a significance level $\alpha = 0.05$:

$$\chi^2 = \sum_{i=0}^{n-1} z_i^2 \,(n_i - 3) - \frac{\left(\left(\sum_{i=0}^{n-1}(n_i - 3)\right)\right)^2}{\sum_{i=0}^{n-1}(n_i - 3)} \quad (5)$$

Where z_i is the Fisher's transform of the correlation coefficients and n_i is the corresponding sample size. For the case of COA, each factor resulting from the sensitivity analysis was both correlated to the reference mass spectra of COA (Crippa et al., 2013) and HOA (Ng et al., 2011a) using R Pearson correlations. Here the chi squared test is performed and verify

the null hypothesis H_0 = all the correlation coefficients are the same. If H_0 can't be rejected it means that the two correlations of the average profiles are not statistically different and thus COA profile can be mixed with HOA profile for the given a-value. The runs for which H_0 is rejected were retained and a range of accepted a-values is obtained. Here, we consider an a-value as valid only if 100% of the runs for this a-value get a positive test (i.e., H_0 is rejected). According to the Chi squared test COA was statistically different from HOA for a-values between 0 and 0.2 (Fig. 1a). In the same way HOA mass spectra correlations with reference HOA and reference COA were inspected and showed an accepted range of a-value between 0 and 0.6 (Fig. 1b). It has to be emphasized that HOA a-values did not affect the COA separation in the selected range, and vice versa (Figure A6).

As Sh-IndOA is specific to the environment of Marseille, reference

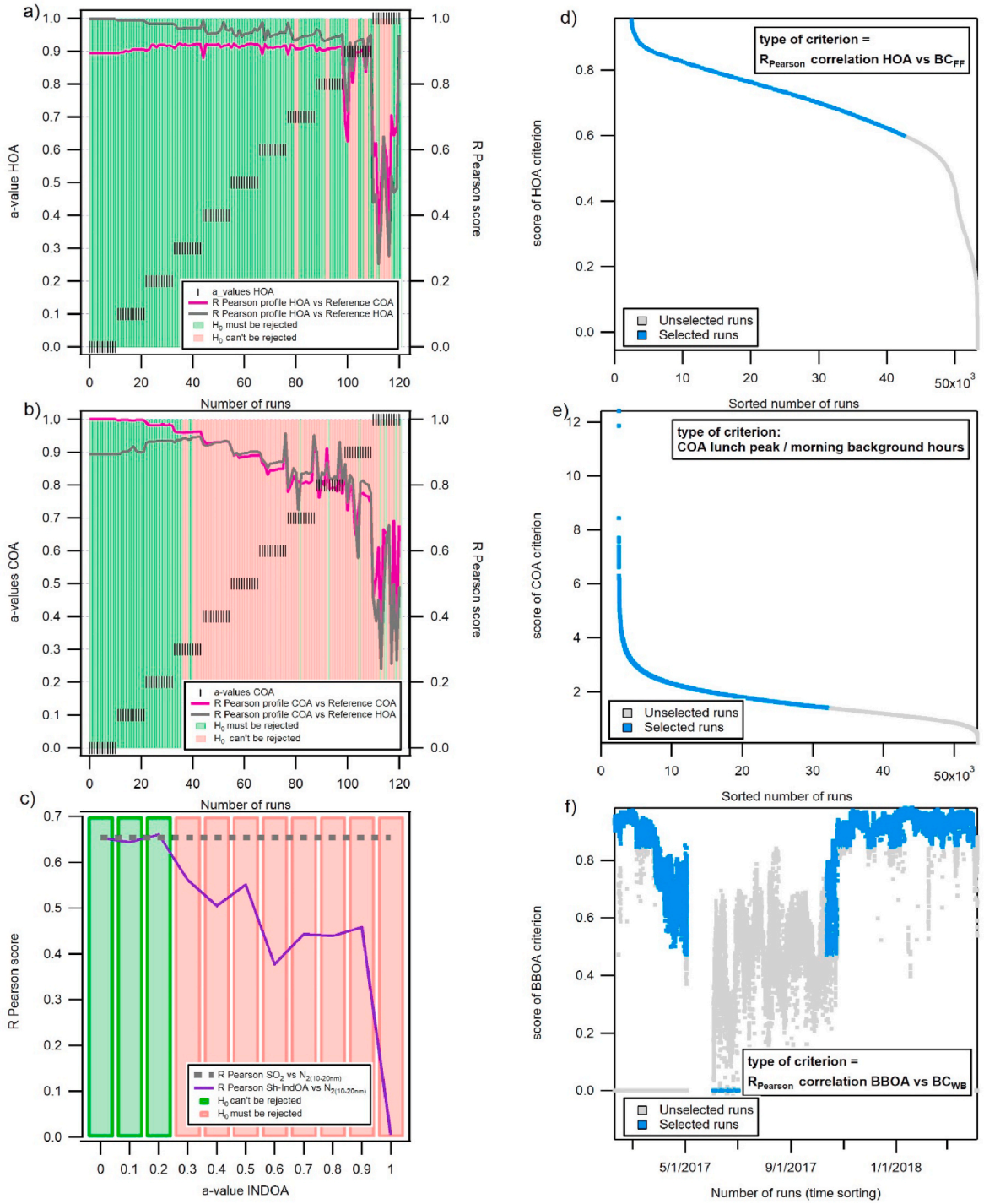

Fig. 1. Sensitivity and Chi squared test results for HOA (a), COA (b) and Sh-IndOA (c). Green bars correspond to the runs with significant a-values and red bars to the rejected runs with wrong a-values according to the Chi squared test results. Rolling PMF runs of all scores (grey points) are displayed for the three criteria: correlation between HOA and BC_{FF} (d), optimization of the ratio of COA lunch peak (e) and correlation between BBOA and BC_{WB} (f). Scores fulfilling the applied thresholds (blue points). For (f) the values set to 0 correspond to the 5 factors runs where there is no BBOA evaluation. (For interpretation of the references to color in this figure legend, the reader is referred to the Web version of this article.)

mass spectra in the literature are scarce. Therefore, we have constrained the factor time series using SO_2 concentrations, as SO_2 can be considered as a specific tracer for industrial and shipping plumes. In addition, we have used the fine particle number between 10 and 20 nm, $N_{(10–20nm)}$, to support the PMF results for the Sh-IndOA factor, as industrial and shipping plumes are characterized by formation of new particles from the condensation of primary or secondary sulfuric acid (Burtscher, 2005; González et al., 2011). Because traffic can be an important source of fine particles, we have estimated the traffic contribution to $N_{(10–20nm)}$, $N_{ff(10–20nm)}$, using BC_{FF} as a tracer and following the methodology of (Rodríguez and Cuevas, 2007). The particle number associated with industrial/shipping plumes ($N_{2(10–20nm)}$) is then estimated as $N_{(10–20nm)}$-$N_{ff(10–20nm)}$. The estimated fraction corresponded to 90% of the $N_{(10–20nm)}$ number concentration for the summer 2017 period (Chazeau et al., 2021). Sh-IndOA was constrained with SO_2 time series and a-values were investigated. The R Pearson correlations between Sh-IndOA and SO_2 were compared to the fixed R Pearson correlation between SO_2 and $N_{2(10–20nm)}$ time series. If H_0 can't be rejected the test will be positive and the a-value will be considered to be valid. The results are displayed in Fig. 1c and a-values resulted to be statistically significant between 0 and 0.2.

A window of 2 weeks shifting by one day was selected based on Canonaco et al. (2021), Parworth et al. (2015) and Tobler et al. (2021). The rotational ambiguity of the PMF results was explored by a bootstrap approach (Efron, 1979) combined with random a-values. Bootstraps recreate new input matrices (2 weeks in length) with randomly selected time points that are used as PMF inputs. The variability in the bootstrap solution is considered as our best estimates for the rotational and statistical uncertainties. With the bootstrap strategy 63 repeats ($7 \times 3 \times 3$) for a given PMF window run are needed to cover the a-value space. Due to the absence of BBOA during some periods PMF runs with both 5 and 6 factors are conducted. In sum, 53,298 runs (423 days $\times$ 63 repeats $\times$ 2) were examined through specific criteria described in the following section.

3.3. Post-analysis with predefined criteria selection

In order to provide efficient evaluation of thousands PMF runs a set of criteria defined within 'SoFi Pro' was used. Here, three criteria were applied for HOA, COA and BBOA, while for the three other factors (Sh-IndOA, LOOA and MOOA) all runs were considered to be "good" due to the lack of specific tracers. BC_{FF} is a pure tracer for traffic, thus the Pearson correlation coefficient between the diurnal cycle of HOA and BC_{FF} is used as first criterion. For COA, the ratio between the lunch peak (11h00 and 12h00 UTC) and the average background concentration in the morning (06h00-08h00 UTC) was used as criterion. This ratio is expected to be above one when cooking emissions are well separated; a score below this value would indicate a contribution from HOA during morning rush hour peaks. BC_{WB} was used to evaluate BBOA. The R Pearson correlation between BC_{WB} and BBOA time series is inspected. If BBOA has not been identified according to this criterion, then a 5-factor solution was selected instead of the 6-factor solution. The scores of the three criteria are presented in Fig. 1 (d,e,f) for all the 53,298 runs.

Statistical thresholds must be applied for each score in order to differentiate the "good" and "bad" runs. A significant drop of the lowest score plots (displayed in descending order in Fig. 1d and e) indicates some rare unstable solutions which might include mixing within the factors. As first data cleansing, the corresponding runs are removed. For the remaining runs of HOA and COA criteria thresholds have to be chosen based on a statistical assessment. The time series of HOA and BC_{FF} were resampled together by bootstrap and the Pearson correlation coefficient was evaluated for each resample. The time series of COA were also bootstrapped and the lunch ratio evaluated each time. It turns out that this statistical method is relevant since the resulting variance of the distributions can be used as threshold of acceptance for the runs. Here 1000 resamples were conducted to evaluate the spread of the designed scores (R Pearson between HOA and BC_{FF} and the COA lunch ratio). The 10th percentile results are used as lower boundaries for both HOA and COA criteria (Canonaco et al., 2021). The distributions for each criterion score evaluated from bootstrap resamples are shown in Figure A7. On the basis of these considerations, the runs presenting correlation coefficients between HOA and BC_{FF} time series under 0.62 and COA lunchtime ratio below 1.45 were not selected.

The BBOA criterion scores (correlation coefficients between time series of BC_{WB} and BBOA) displayed high values for the cold period, while the correlations appear to be poor for summer (Fig. 1f). This source is expected to be significantly reduced in this period as there is no domestic heating and no wildfire event recorded with the ACSM. Even if the correlation is high for some summer events (i.e. from 6 to August 17, 2017), the related runs are not selected as their time period was shorter than the time window length and won't be properly modelled by PMF. During the transition periods (i.e. April and October 2017), the scores had intermediate values, and applying restrictive criteria to these scores leads to higher residuals in the final solution. Since the three periods should be treated separately, the criteria thresholds are resolved differently than for HOA and COA. To assess the boundary between all BBOA scores Fisher transformed correlation coefficients Z' were calculated:

$$Z' = 0.5 \times \ln\left(\frac{1+R}{1-R}\right) = \arctan(R) \quad (6)$$

where R is the Pearson correlation coefficient between BBOA and BC_{WB}. The calculation was performed through 3 time classes: the period from end of spring to begin of autumn 2017 noted as "bad values", the April and October 2017 months for "transitional values" and the rest of the study period referred as "good values". The results are displayed in Figure A8. A Gaussian shape peak fitting can be performed on each Z' data which are normally distributed. The fitted Z' data of "significant BBOA" (green) and "transitional BBOA" (yellow) are converted to standard normal distribution (see Figure A9 and details in SI text). Following the HOA and COA criteria threshold determination the 10th percentile results are used as lower boundaries for BBOA criteria. A $P_{0.1} = 1.24$ for the "significant BBOA" and $P_{0.1} = 0.51$ for the "transitional BBOA" were found. The Z' values were then transformed back to R Pearson as follow:

$$R = \frac{e^{2Z'} - 1}{e^{2Z'} + 1} \quad (7)$$

We determined runs with scores below R = 0.845 for "significant BBOA" and R = 0.47 for "transitional BBOA" were not selected. The factor was also inspected using the explained variation of m/z 60 by BBOA (Figure A10). The runs with an explained variation significantly lower than those of other factors were not considered, which didn't improve the previous selection.

At the end the criteria list discarded 19.6% of runs with HOA criterion, 39.1% with COA criterion and 55.6% with BBOA criterion. All the runs fulfilling the entire criteria list are selected and averaged into one unique solution with time-dependent factor profiles.

4. Results and discussions

PMF results displayed abnormal high concentrations from 2 to February 13, 2018 in contrast with the measured concentrations. Therefore the corresponding runs were removed from the definitive solution. In total 20.6% of the PMF runs were retained after the criteria selection and the resulting solution includes a minimum amount of non-modelled time-points representing 2.4% of the total number of measurements.

4.1. Residuals and factors uncertainties

The residuals distribution was examined in order to detect some systematic under or overestimation of the data points. Figure A11 displays the scaled residuals over the m/z (a) and the time (b). Scaled residuals scattering in the −3 to +3 range for the whole solution attest to the validity of the PMF results (Canonaco et al., 2021; Paatero and Hopke, 2003). Only 1.8% of the residuals were out of range, highlighting the good quality of the solutions. Some brief periods with high residuals are identified and correspond mostly to two cases. First, scaled residuals can increase for the periods before and after technical problems on ACSM instrument (e.g. unstable air beam signal after the reset of ACSM in 20–21 July 2017). Several interruptions led to probable instability in the organic signal which can't be explained by the PMF results. Second, scaled residuals were higher for specific episodes of fast environmental changes (e.g. wind shifting loading polluted air mass). This feature happened especially during the cold period (25 October; 27–29 November; 24–26 December; 12 January) when nocturnal breezes advected instantly intense OA concentrations, mostly from biomass burning origin. These events of high residuals were short in time (less than 1–2 days) and a 14 days PMF window could be insufficient to capture the OA composition during these episodes (Canonaco et al., 2021). Overall, the residuals pattern indicated a good PMF solution and provides a Gaussian-shaped distribution presented in Figure A11c. In this figure the scaled residuals were approximately normally distributed around 0 with a reduced spread.

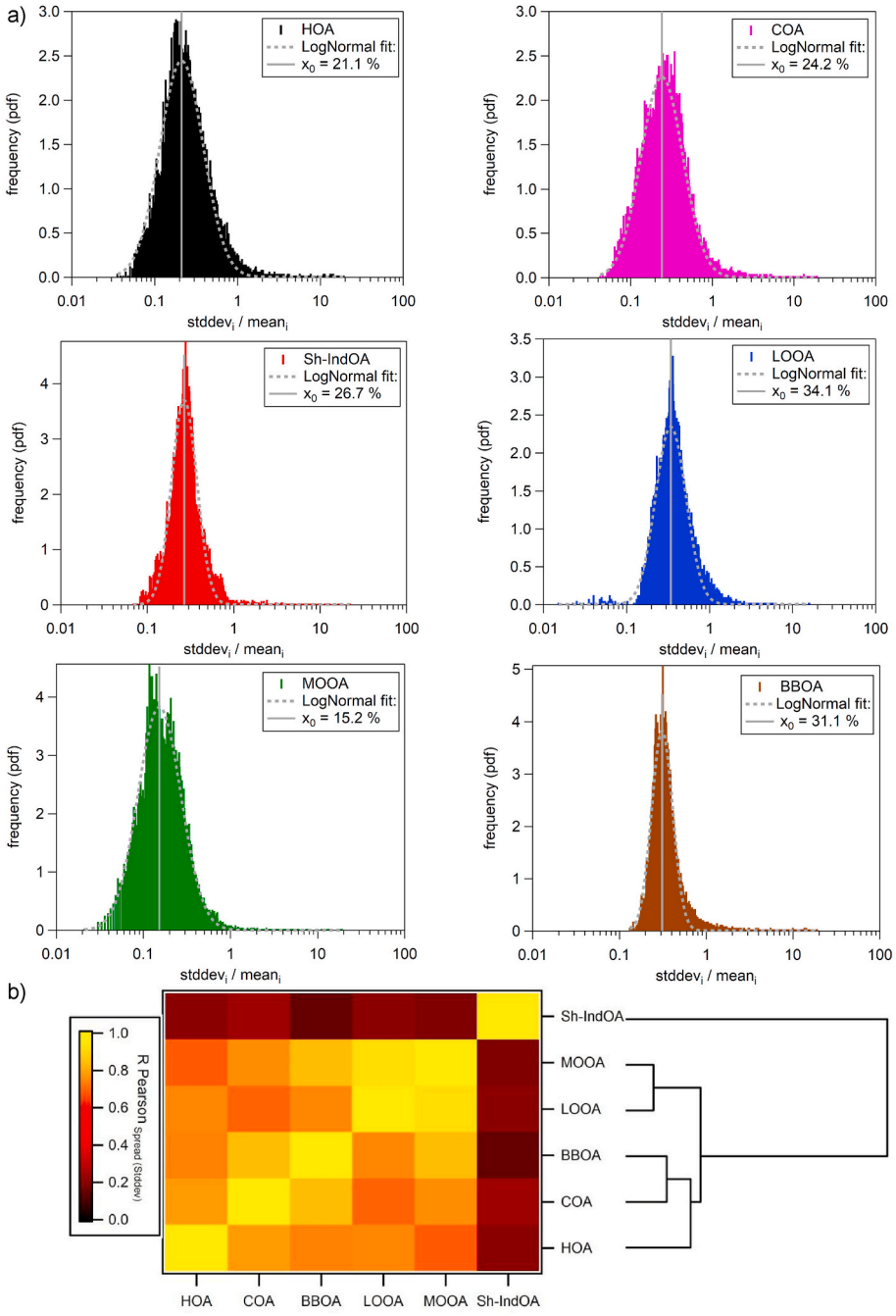

Fig. 2. PMF error estimation for the 6 factors (a). The standard deviations divided by the mean concentrations of each PMF time points are represented as log-probability density functions. X0 values are the centres of the lognormal fits. The graph below represents the correlation matrix of R Pearson between the spread (standard deviation) of PMF factors time points (b). A hierarchical clustering is performed over the matrix and is represented as dendrogram.

PMF uncertainty for each factor was assessed from the variability of time-point repeats obtained by the selected rolling runs. It has to be noticed that this PMF error accounts for the variability from bootstrap resampling and repeats provided by the different a-value combinations. Fig. 2a represents the probability density function (pdf) of the standard deviation divided by the mean concentrations for each PMF time points. Similarly to Canonaco et al. (2021) and Tobler et al. (2021), error values for PMF factors are expressed as the center of the lognormal fit (x_0) from each log-distribution. The average error was ±21.1%, ±24.2%, ±26.7%, ±34.1%, ±15.2% and ±31.1% for HOA, COA, Sh-IndOA, LOOA, MOOA and BBOA, respectively.

The Pearson correlation between the respective factors standard deviations of PMF time points is assessed in Fig. 2b. A hierarchical clustering was performed on the resulting correlation matrix to evaluate uncertainties of the factors splitting or mixing. A high correlation between the standard deviations might indicate instability in the factors separation. This analysis was also performed for each season (Figure A12). Two clusters are assessed, including LOOA and MOOA in the first one and BBOA, COA and HOA in the second one. Sh-IndOA is excluded from the two patterns as the factor is constrained with a specific marker. LOOA and MOOA are gathered in a same cluster for all season. This dependence was also tested by calculating the cosine similarities between standard deviations of factors time points (Figure A13). The strong collinearity observed between LOOA and MOOA might indicate that a clear separation remains uncertain.

4.2. Rolling vs seasonal PMF results

An inter-comparison with seasonal PMF method was achieved over the study period to inspect the validity of the rolling PMF analyses. The description of PMF methodology applied to every season is presented in the supplementary. The comparison between seasonal and rolling PMF time series for each factor is shown in Figure A14. A good agreement was found for the 3 constrained factors with significant correlation coefficient R^2 (0.88 for HOA, 0.75 for COA and 0.72 for Sh-IndOA) and slopes (determined from orthogonal distance fits) close to 1 (0.90 for HOA, 0.98 for COA and 1.09 for Sh-IndOA). For MOOA, results were also satisfactory (R^2 = 0.83; slope = 0.83), but data points are more dispersed especially for the winter period. BBOA showed moderate correlations (R^2 = 0.52) and slope of 1.15. This value is mainly increased due to a steeper slope for winter data points, suggesting an underestimation of the seasonal PMF. LOOA comparison revealed an inverse trend for winter with an overestimation of the seasonal PMF. Overall, for LOOA, results are different between the seasonal and the rolling PMF (R^2 = 0.23). The LOOA profiles were very different between seasons, indicating that the seasonal PMF cannot capture the continuous evolution in the oxygenated fraction.

A comparison between the scaled residuals from seasonal and rolling PMF is presented in Figure A15. For each season the scaled residuals were normally distributed around 0 with both methods. However the rolling PMF showed lower scaled residuals compared to conventional seasonal PMF, as settled by the narrower width of the Gaussian fits (2.40 vs 2.54, 2.37 vs 2.65, 3.28 vs 3.31, 3.25 vs 4.04 for spring, summer, autumn and winter, respectively) (Table A2).

4.3. Interpretation of PMF factors

In this section the averaged source apportionment solution is investigated with factor profiles presented in Fig. 3, their R^2 correlation with literature references (Figure A16) and the R^2 correlation between the factors time series (Table A3). Figure A17 shows the factors time series, while the monthly mass concentrations of the factors and their seasonal relative fractions are displayed in Fig. 4. The factors relative diurnal cycles and their respective relation with external proxies are shown in Fig. 5. Finally Table 1 summarizes the correlation coefficient (R^2) between the factors and external markers measured over the study time period.

HOA. The factor profile constrained based on Ng et al. (2011a) exhibits high contributions from hydrocarbon fragments, including m/z 29 ($C_2H_4^+$), 41 ($C_3H_5^+$), 43 ($C_3H_7^+$, $C_2H_3O^+$), 55 ($C_4H_7^+$), 57 ($C_4H_9^+$), 69 ($C_5H_9^+$) and 71 ($C_5H_{11}^+$). For the heavy fragments we denote a meaningful contribution (40% of the total fragment) of the PAH m/z 202 known to derivate from the pyrene (Dzepina et al., 2007). The averaged a-value for this factor was 0.3 and varying between P_{10} = 0.2 and P_{90} = 0.5 (Figure A18). HOA contribution is constant through the seasons with values in the range of 9.2–12.1% and concentrations between 0.46 and 0.7 μg m^{-3}. This contribution appears to be lower than previous Marseille OA source apportionment studies in summer 2008 (19.4%; El Haddad et al., 2013) and in the 2011–2012 period (17%; Bozzetti et al., 2017a). While this difference can be attributed to cleaner exhaust emissions, it is worth noting that the analysis from El Haddad et al. (2013) was performed over a shorter period (2 weeks) and a COA factor couldn't be resolved from HOA leading to higher HOA contribution. The factor diurnal profile shows a bimodal pattern of traffic emissions with a morning peak maximum at 6–7h UTC and an evening peak maximum at 18h UTC (Fig. 5). BC_{FF} and NO_x concentrations display similar diurnal

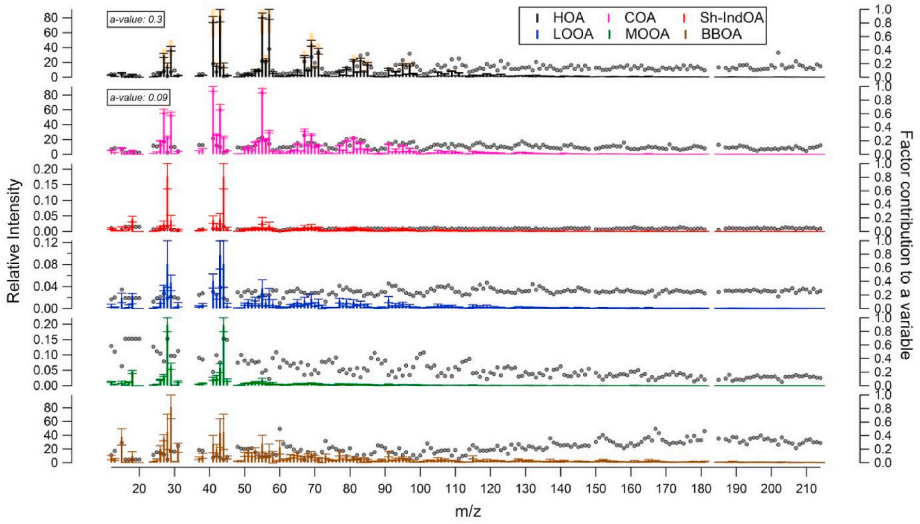

Fig. 3. Average mass spectra profiles for the 6 factors solution. Error bars indicate the standard deviation of each profile through the study period. Grey dots show the factor contribution to every organic fragment.

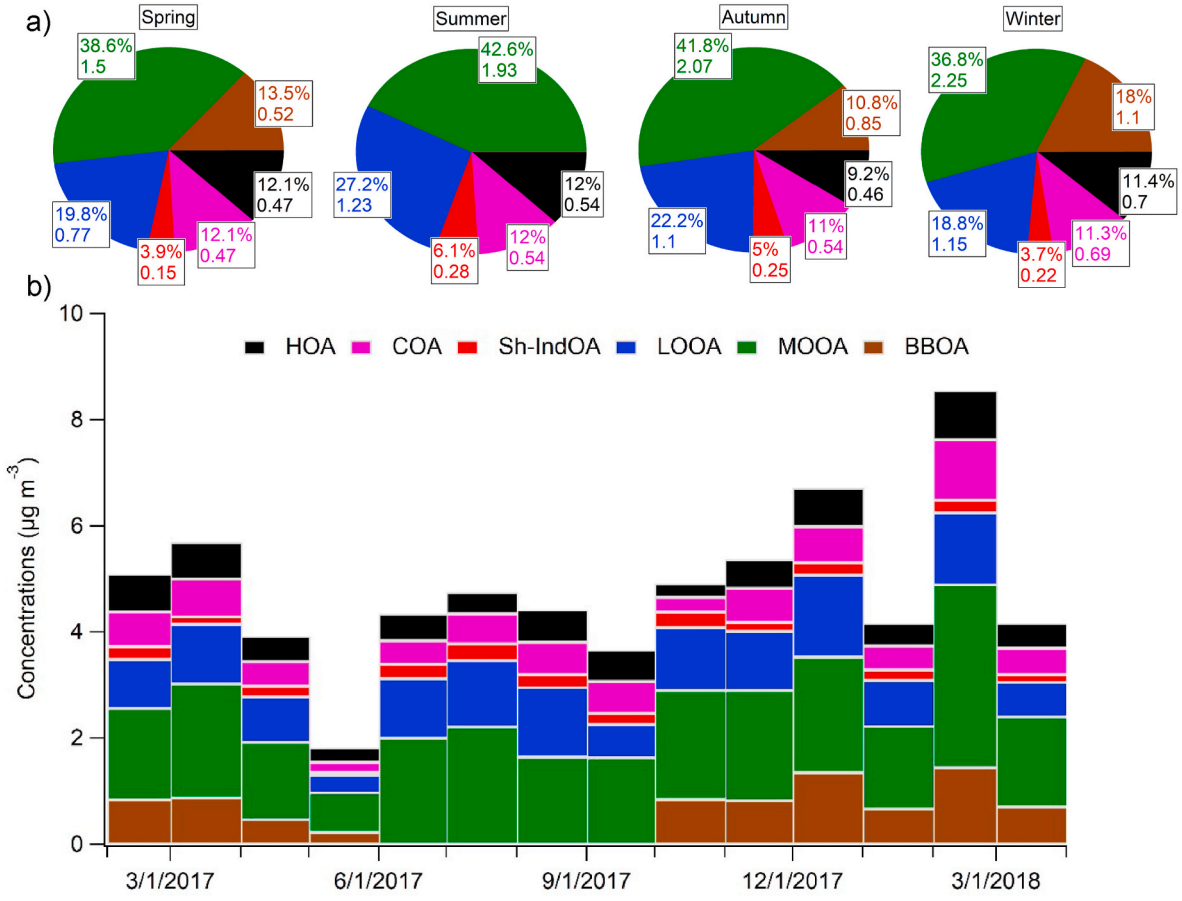

Fig. 4. Seasonal pie chart contributions (a) and monthly factors concentrations (b) for the full period. The pie chart contributions are indicated in percent and the mean concentrations in µg m^{-3}.

features and their time series are well correlated with HOA ($R^2_{HOA\ vs\ BC_{FF}} = 0.45$ and $R^2_{HOA\ vs\ NOx} = 0.5$; Table 1). The average ratio of HOA to BC_{FF} determined with the slope from orthogonal distance regression (Figure A19) is 0.47 (and intercept = −0.09), which was consistent with values for the same station (0.4; El Haddad et al., 2013) and for Paris (France) stations (0.37 and 0.61; Crippa et al., 2013). This ratio can also be compared to values found for tunnel measurements at very low OA concentrations (Chirico et al., 2011).The average ratio of HOA to NO_x is 0.012 (intercept = 0.09) which is in agreement with (Bozzetti et al., 2017a) for the same station (0.023) and with (Favez et al., 2010) for Grenoble (France) station (0.02). The slope was higher for summer data (0.019) due to the reduced lifetime of NO_x linked to higher hydroxyl radical (OH) concentrations occurring in this season (van der A et al., 2008). According to correlation analysis in Table 1, HOA concentrations seem to be associated with ultrafine particles with a predominance in the 70–100 nm range.

COA. COA profile kept the same features than its constraint from Crippa et al. (2013) and the major fragments are similar from those of HOA profile although m/z 41 to 43 and m/z 55 to 57 ratio appeared higher. An averaged a-value of 0.09 was used for the constraint. As no markers are available in this study the COA signature was inspected through the diurnal cycle which showed an apparent lunch peak at 11h UTC and a dinner peak at 19h UTC (Fig. 5). COA contributions of ~11.5% were constant throughout the seasons (0.47–0.69 µg m^{-3}). It is in a similar range than other urban sites in Europe like in London (8%; Reyes-Villegas et al., 2016), Athens (10%; Stavroulas et al., 2019) or Barcelona (16% in early Spring; Mohr et al., 2012). In Marseille Bozzetti et al. (2017a) resolved much lower contributions for COA (4%), which could be explained by the weak time resolution of offline AMS (one day) as it did not enable the COA separation based on the diurnal cycle. Another major issue was the low solubility of COA for the offline AMS analysis, causing high uncertainties for this factor (Daellenbach et al., 2016). COA concentrations were associated to size distribution between 70 and 200 nm (Table 1).

Sh-IndOA. This factor accounts for the organic fraction related to industrial and shipping activity that are prominent in the Marseille region. The average a-value was 0.1 with a very shallow distribution (Figure A18). Previously El Haddad et al. (2013) and Bozzetti et al. (2017a) resolved a similar factor at the MRS-LCP station attributed to the industrial emissions from the Fos-sur-mer petrochemical area (North-West). During these studies the factor was correlated to heavy metals and PAHs advected on site by sea breezes in the late morning. Here for the Sh-IndOA factor we consider an additional influence of shipping emissions from the Marseille harbour. The resulting plumes are strongly associated with SO_2 and UFPs concentrations as described by Chazeau et al. (2021). As the factor time series were constrained with the SO_2 concentrations, Sh-IndOA displayed a similar diurnal pattern to SO_2 with an increase at 7–8h UTC followed by a slow decrease through the day (Fig. 5). The average ratio of Sh-IndOA to SO_2 from the slope in Figure A19 was 0.10 and was very stable through the seasons. Sh-IndOA profile resembles a highly oxygenated organic aerosol, with dominance of m/z 44 (CO_2^+) and m/z 28 (CO^+) (Fig. 3). As mentioned by El Haddad et al. (2013) this factor might include secondary organic aerosols fraction due to the photochemical aging during the plumes transport towards the station. The seasonal contribution is estimated to 3.7–6.1% (0.15–0.28 µg m^{-3}) with higher concentrations in summer because of higher photochemical activity and favourable air mass circulation (El Haddad et al., 2011b). Similar contributions were found with AMS measurements for 2 weeks in summer 2008 (6.2%; El Haddad et al., 2013). However, Bozzetti et al. (2017a) resolved with offline AMS a

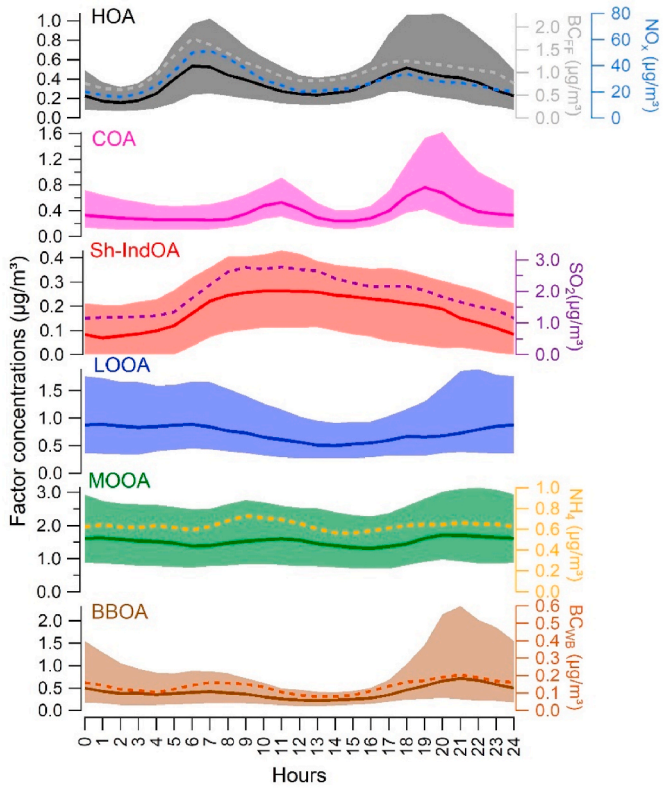

Fig. 5. Median diurnal cycles for the 6 factors (solid lines). The shaded areas show the 25th – 75th percentiles range. Dashed lines represent some external tracers: BC_{FF} (grey), NO_x (blue), SO_2 (violet), NH_4 (yellow) and BC_{WB} (light brown). (For interpretation of the references to color in this figure legend, the reader is referred to the Web version of this article.)

Table 1
R^2 correlation coefficients with a 95% confidence interval between solution factors and external data recorded at MRS-LCP. Numbers in bold represent significant correlations.

R^2 Pearson	HOA	COA	Sh-IndOA	LOOA	MOOA	BBOA
Cl^-	0.1	0.08	0	0.08	0.13	0.12
NH_4^+	0.05	0.06	0.03	0.11	**0.44**	0.05
SO_4^{2-}	0.01	0.01	0.1	0.03	0.21	0
NO_3^-	0.1	0.1	0	0.15	**0.43**	0.11
$NO_{3,org}$	0.13	0.14	0	0.23	**0.44**	0.17
$NO_{3,inorg}$	0.08	0.08	0	0.11	**0.39**	0.08
BC_{WB}	0.28	0.35	0	0.31	0.29	**0.76**
BC_{FF}	**0.45**	0.19	0.05	0.31	0.17	0.16
m/z 43	0.47	0.54	0.04	**0.61**	0.58	0.53
m/z 44	0.24	0.37	0.06	0.56	**0.83**	0.58
m/z 55	0.65	**0.67**	0.04	0.57	0.46	0.68
m/z 57	**0.73**	0.53	0.03	0.48	0.32	0.59
m/z 60	0.33	0.46	0	0.36	0.39	**0.88**
NO_2	**0.49**	0.26	0.06	0.35	0.17	0.27
NO	**0.35**	0.08	0.02	0.2	0.07	0.16
NO_x	**0.5**	0.18	0.05	0.32	0.13	0.24
O_3	0.23	0.13	0	0.24	0.07	0.26
SO_2	0.03	0.01	**0.82**	0.01	0.01	0
CO_2	0.25	0.17	0	0.29	0.2	**0.42**
CH_4	0.18	0.14	0	0.21	0.21	**0.31**
N (20–30 nm)	0.22	0.11	0.05	0.11	0.02	0.1
N (30–50 nm)	0.35	0.22	0.08	0.23	0.07	0.22
N (50–70 nm)	**0.47**	0.34	0.09	0.39	0.18	0.42
N (70–100 nm)	**0.5**	**0.41**	0.07	0.48	0.31	**0.6**
N (100–200 nm)	0.46	**0.41**	0.05	**0.53**	0.46	**0.7**
N (200–1000 nm)	0.34	0.34	0.04	0.48	**0.61**	0.53

higher fraction of 17% for industrial factor, which was mainly driven by a strong event in February 2012. The low contribution to organic aerosol for this source is expected as the plumes are mostly attributed to UFPs and thus influence particle mass concentrations only to a minor extent (Chazeau et al., 2021).

BBOA. BBOA was identified from mass spectral fingerprints with high contribution to m/z 60 ($C_2H_4O_2^+$) and m/z 73 ($C_3H_5O_2^+$) fragments which are originated from anhydrous sugar fragmentation (Alfarra et al., 2007). BBOA profile in this solution is comparable with those from literature (Crippa et al., 2014; Ng et al., 2011a). This factor shows expected features like high correlations with BC_{WB} and is one of the most important sources in winter with a contribution of 18% (1.1 µg m^{-3}). BBOA is missing in summer and contributions ranged between 10.8 and 13.5% (0.52–0.8 µg m^{-3}) for the rest of the year (Spring and Autumn). These values are comparable to other Mediterranean urban sites (10% in winter at Athens; Stavroulas et al., 2019), 11% in spring at Barcelona; Mohr et al. (2012). Still Bozzetti et al. (2017a) found much higher contribution for this site in winter (43%) attributed to elevated open burning emissions occurring at night during this period. BBOA was characterized by an intense peak in the night advected with N-E land breezes combined with the decrease of boundary layer height (Chazeau et al., 2021). During these periods the low background concentrations for BBOA switched to spiking episodes which were 10–15 times higher. BBOA can be associated to well-known markers as levoglucosan (including the derived species galactosan and mannosan) displaying an excellent correlation with $R^2 = 0.80$ (Figure A20). Moreover, the potassium (K^+) fraction which is not related to sea salt is often associated to biomass combustion sources in the cold period. Non-sea-salt K^+ (Nss-K^+) concentrations were calculated according to Sciare et al. (2005) and using the Na^+/K^+ ratio of marine-related source determined by Salameh et al. (2018) for PM in Marseille. Nss-K^+ from filters were correlated well with the BBOA factor contribution ($R^2 = 0.55$; Figure A20). The BBOA to BC_{WB} ratio from the literature showed a large variability depending on the burning conditions. Here a value of 2.06 (intercept = 0.02) was found with low seasonal variations (Figure A19) and is consistent to values reported for field studies (Reid et al., 2005). Finally, comparable to COA concentrations BBOA was correlated to size distribution between 70 and 200 nm, a range often attributed to wood burning emissions (Coudray et al., 2009).

Oxygenated OA. The secondary fraction of OA (SOA) was split into the LOOA and MOOA factors. The main difference between the two factors is the higher fraction of m/z 44 to the organic mass for MOOA compared to m/z 43 for LOOA. LOOA profile exhibits strong correlation with SVOOA (Semi-Volatile Oxygenated Organic Aerosol) mass spectra from the literature (Figure A16) whereas MOOA profile resembles more to LVOOA (Low Volatiliy Oxygenated Organic Aerosol). Fractional contribution of m/z 44 (f44) is considered as proportional to the elemental O:C ratio and the later can be assessed following the calculation from Canagaratna et al. (2015). The determined O:C ratios for LOOA and MOOA were 0.43 and 0.93, respectively, which are close to the ratio obtained by El Haddad et al. (2013) (0.33 for SVOOA and 0.84 for LVOOA). For every season MOOA was the largest OA source with 36.8–42.6% (1.5–2.25 µg m^{-3}) followed by LOOA with 18.8–27.2% (0.77–1.23 µg m^{-3}). On a yearly basis, MOOA seems to be more related to ammonium ($R^2 = 0.44$ from Table 1 and diurnal profile in Fig. 5). Even if MOOA is expected to be related to aged background aerosol, the correlation with sulfate concentrations is less clear for every season (Table A4). This is probably due to some contribution from Sh-IndOA assigned to direct sulfate emissions. Furthermore, the MOOA diurnal profile was mostly flat suggesting the long-range transport origin for this factor, except for winter profile which shows, as for all OA factors, increased concentrations at night under a shallow boundary layer (Figure A21). In overall LOOA does not show significant correlation with semi volatile species such as particulate nitrate. The fact that LOOA variability is not driven by its volatility prevents here to use the SVOOA denomination like other studies (Jimenez et al., 2009; Lanz et al., 2007).

MOOA displayed a stronger correlation with nitrate ($R^2 = 0.43$) than LOOA ($R^2 = 0.15$). It has to be noted that organic nitrate concentrations ($NO_{3,Org}$) of this dataset were previously estimated for the nitrate functionality only following Farmer et al. (2010) and Kiendler-Scharr et al. (2016) recommendations. Correlations were more pronounced for $NO_{3,Org}$ than for $NO_{3,Inorg}$ which is exclusively attributed to ammonium nitrate. The summer period exhibited a different trend and only the correlation between LOOA and $NO_{3,Org}$ was evident with $R^2 = 0.53$ (Table A4). Several studies highlighted the reaction of biogenic VOCs with nitrate radicals at night-time as an important source of particulate organic nitrates and by inference of OA (Fry et al., 2013; Kiendler-Scharr et al., 2016; Xu et al., 2015). This is supported by the summer diurnal profile which displayed maximum at 3–4h UTC in the night (Figure A21) and the enhanced biogenic emissions in the region in summer (El Haddad et al., 2013; Parra et al., 2004). A complete description of the whole secondary inorganic aerosols and the $NO_{3,Org}$ fraction during the study period can be found in Chazeau et al. (2021). LOOA concentrations were affiliated to a large size range between 100 and 1000 nm, while MOOA considered as more oxidized is linked to particles up to 200 nm.

4.4. Insights into the BBOA and SOA origins

Unlike known anthropogenic factors which were directly attributed to a single source (i.e. HOA, COA and Sh-IndOA), BBOA and SOA (LOOA and MOOA) may exhibit different origins depending on the time period. Bozzetti et al. (2017a) proposed that BBOA originates from multi-sources of biomass burning. The authors revealed an evolution in BBOA composition, with combustion of cellulose-rich materials attributed to agricultural waste burning during spring and late autumn and a domestic heating origin over winter period. Salameh et al. (2018) also described this separation from a PMF analysis of organic and inorganic markers. Moreover, Bozzetti et al. (2017a) mentioned secondary biomass burning compounds such as nitrocatechols attributed to the BBOA factor. In the present study the averaged mass spectra showed a significant contribution of m/z 44 to BBOA (Fig. 3) supporting the assumption of secondary compounds included in primary BBOA factor. We explore the f44 vs f60 space for the BBOA profile to investigate the aging of BBOA during the different seasons (Fig. 6). While the main points scatter in the fresh biomass burning space (f60 ≈ 0.2–0.35 and f44 < 0.06) and are associated with low temperatures, two trends showed negative slopes associated with increasing temperatures and corresponded to mid-spring and late autumn periods. These slopes

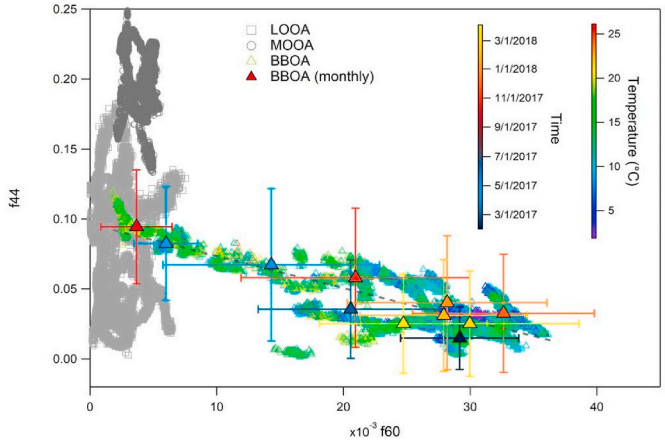

Fig. 6. f44 vs f60 ratio for BBOA factor profiles (color-coded according to the temperature). The solid triangles with error bars are for BBOA factor profiles with a monthly resolution and are color-coded according to the time. The dark grey circles and light grey squares represent the ratio of MOOA and LOOA factor profiles, respectively. (For interpretation of the references to color in this figure legend, the reader is referred to the Web version of this article.)

reflect the increasingly oxygenated nature of BBOA probably with aging as the biomass burning plumes show a trend toward higher f44 and lower f60 values with age. This may be linked to levoglucosan oxidation exposed to hydroxyl radicals (OH) at increasing temperature or the condensation of secondary formed in BBOA plumes (Cubison et al., 2011; Hennigan et al., 2010). These aged BBOA components could also be related to the regional transport of agricultural and domestic green waste burning from the surroundings, as expected in this area during spring and autumn (Chazeau et al., 2021; Fountoukis et al., 2014).

The f44 vs f43 space is a common diagnostic tool used to distinguish the secondary factors variability according to their atmospheric aging (Ng et al., 2010). Here, contributions from other sources (i.e. HOA, COA, Sh-IndOA and BBOA) are subtracted from the space to fully capture the SOA variability (Canonaco et al., 2015). The seasonal f44/f43 for SOA measured points and the f44/f43 for the modelled factor profiles (LOOA and MOOA) are shown in Fig. 7. SOA points scatter in the form of lines instead of clouds and extend beyond the modelled LOOA and MOOA points, except for the December period which showed a distinct cloud (Figure A22). An underestimation of the m/z 43 signal was recorded after an unknown technical issue with the ACSM for this one-month period (see SI text). These data points were excluded from the f44/f43 analysis. The data points in Fig. 7 lie in different location in f44/f43 space depending on the seasons similarly to other studies (Canonaco et al., 2015; Crippa et al., 2014; Freney et al., 2011; Reyes-Villegas et al., 2016). Furthermore, the points from the modelled factor profiles display high variability in space mostly for LOOA. This implies that a yearly or seasonal PMF solution, unless going to higher number of factors, would fail to capture the entire variability of SOA, unlike rolling PMF solution, which provides continuous observations of physico-chemical processes leading to LOOA and MOOA formation. The triangle plot determined by Ng et al. (2010) is also represented in Fig. 7. As expected the more aged MOOA components moved towards the highest point during the aging process while LOOA components were concentrated in the lower half of the triangle. During all seasons the f44 for MOOA and LOOA factors ranges from 0.13 to 0.25 and 0.003 to 0.19, respectively, similarly to values reported by Ng et al. (2010) (0.10–0.25 for LVOOA and 0–0.13 for SVOOA) and Crippa et al. (2014) (0.10–0.26 for LVOOA and 0.05–0.16 for SVOOA).

OA concentrations measured during summer are likely to involve high biogenic activity. El Haddad et al. (2011a) and El Haddad et al. (2013) provide a complete chemical description of SOA and found that non-fossil fraction contributes up to 80% of the total secondary components. SOA data fully lied on the right side of the triangle space and are associated with higher temperature in summer, which is expected for biogenic SOA precursors (Alfarra et al., 2012; Ng et al., 2010; Pfaffenberger et al., 2013). This is in agreement with the study of El Haddad et al. (2013) which estimated a very high contribution of monoterpenes (between 40 and 60%) in the formation of non-fossil SOA. Several processes involving LOOA formation are underlined in this study. Some enhanced concentrations are observed under high oxidant level (Ox; corresponding to the sum of NO_2 and O_3 in ppb; Clapp, 2001) and high temperature conditions (Figure A23). The strong relation between Ox and temperature highlights the active photochemistry linked to the VOCs conversion in LOOA. Yet, the summer diurnal profile in Figure A21 let suppose a contribution from nigh-time chemistry. As mentioned in section 4.3, the oxidation of biogenic VOCs by NO_3 radicals may be a significant pathway for LOOA formation as illustrated by the correlation with $NO_{3,org}$ concentrations. Also, the study of Lanz et al. (2007) showed that condensation of fresh oxygenated organic aerosols was enhanced during the night/early morning following the hot summer days. While MOOA might be transformed from LOOA via OH chemistry during the mid-day (Figure A21), its concentrations also increased at elevated temperature and Ox concentrations (Figure A23), supporting the potential direct conversion of VOCs to MOOA (Canonaco et al., 2015). It has to be noted that the September month displayed the same features described previously (Fig. 7) as its meteorological conditions

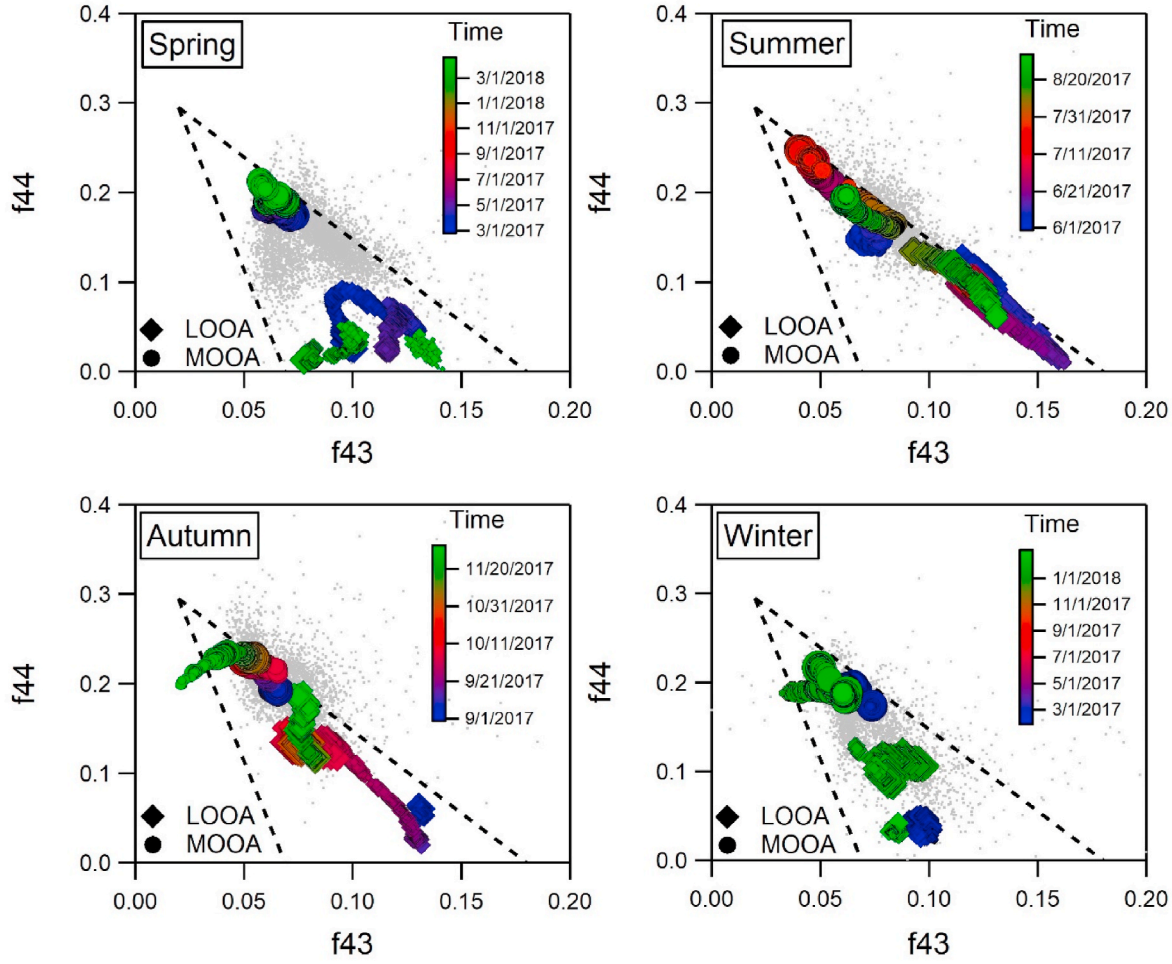

Fig. 7. SOA f44 vs f43 space for each season. The data points are determined by subtracting the f44 and f43 contributed from the other factors and are color-coded according to the OA mass concentrations. The modelled ratio for LOOA (diamonds) and MOOA (circles) points are color-coded based on the temperatures and the size of markers is proportional to the factor contributions. The grey dashed lines are the triangle boundaries set by Ng et al. (2010). (For interpretation of the references to color in this figure legend, the reader is referred to the Web version of this article.)

were comparable to the summer period.

Data for winter, spring and autumn scattered within the f44 vs f43 triangle space and were expected to arise from anthropogenic sources. Laboratory studies on SOA formation from biomass burning emissions tend to be located on the left side of the triangle (Ahern et al., 2019; Hennigan et al., 2011; Heringa et al., 2011) whereas those from vehicular exhaust are focused in the lower center part (Canonaco et al., 2015; Tkacik et al., 2014). The temporal variation of LOOA fragments profiles (m/z 60 and m/z 57) was inspected in Figure A24. Some episodes of increasing m/z 60 contributions occurred in winter and spring, corresponding to enhanced R^2 correlation between LOOA and BC_{WB}. The highest episodes were in December with the maximum m/z 60 contribution coinciding with the Christmas event, a polluted period mostly linked to biomass burning from domestic heating (Chazeau et al., 2021). It corresponded to a reduced m/z 43 in LOOA factor and data tended to the left part of the f44/f43 triangle (Figure A22). However, as stated earlier, the ACSM issue on m/z 43 from December could distort this analysis. Added to that, m/z 57 from LOOA showed strong seasonal variations with high values in autumn, winter and spring, supported by the R^2 correlation with BC_{FF} and highlighted the traffic origin for LOOA (Figure A24b). Added to that, the diurnal profiles during these seasons (Figure A21) exhibited a peak as the same time as morning traffic rush hour, suggesting a contribution from fast oxidation of freshly emitted primary OA. For MOOA, the concentrations slightly increased at night as they were driven by meteorological features such as boundary layer height, wind circulation, temperature and humidity (Figure A25) during winter and spring period. The high degree of aging for the oxygenated MOOA presumes some distant sources of OA emission advected through long-range transport. Daellenbach et al. (2017) already mentioned the regional origin of SOA concentrations in winter which were correlated at several sites on the Swiss plateau.

Fig. 8a presents the seasonal wind rose occurrences for each season. The seasonal wind analysis of HOA, COA, Sh-IndOA, BBOA and LOOA were further described in the SI (Figure A26). In summary, the wind analysis for HOA and COA displayed pattern with high concentrations due to local emissions related to comparably low wind speeds. During winter and autumn highest concentrations were mostly observed from the North-East when land breeze prevails. These air masses developed at night and brought the OA concentrations, emitted during the day, back to the city. In the same time land breeze advected BBOA concentrations (Figure A26) from surrounding suburban residential areas of Marseille (Chazeau et al., 2021). As expected, the Sh-IndOA dynamic was driven by the south-westerly sea breeze at each season which brought the mixed industrial and shipping plumes from Fos-sur-mer area and the harbour to the city. LOOA factor appears to have the same local origin as the summed primary factors (i.e. HOA, COA and BBOA) for spring, autumn and winter. In summer, when the concentration assumed to stem from biogenic activity at night, LOOA displayed a North to East origin from inside the lands. MOOA displayed very contrasted situations and the related seasonal NWR analysis plots are represented in Fig. 8a.

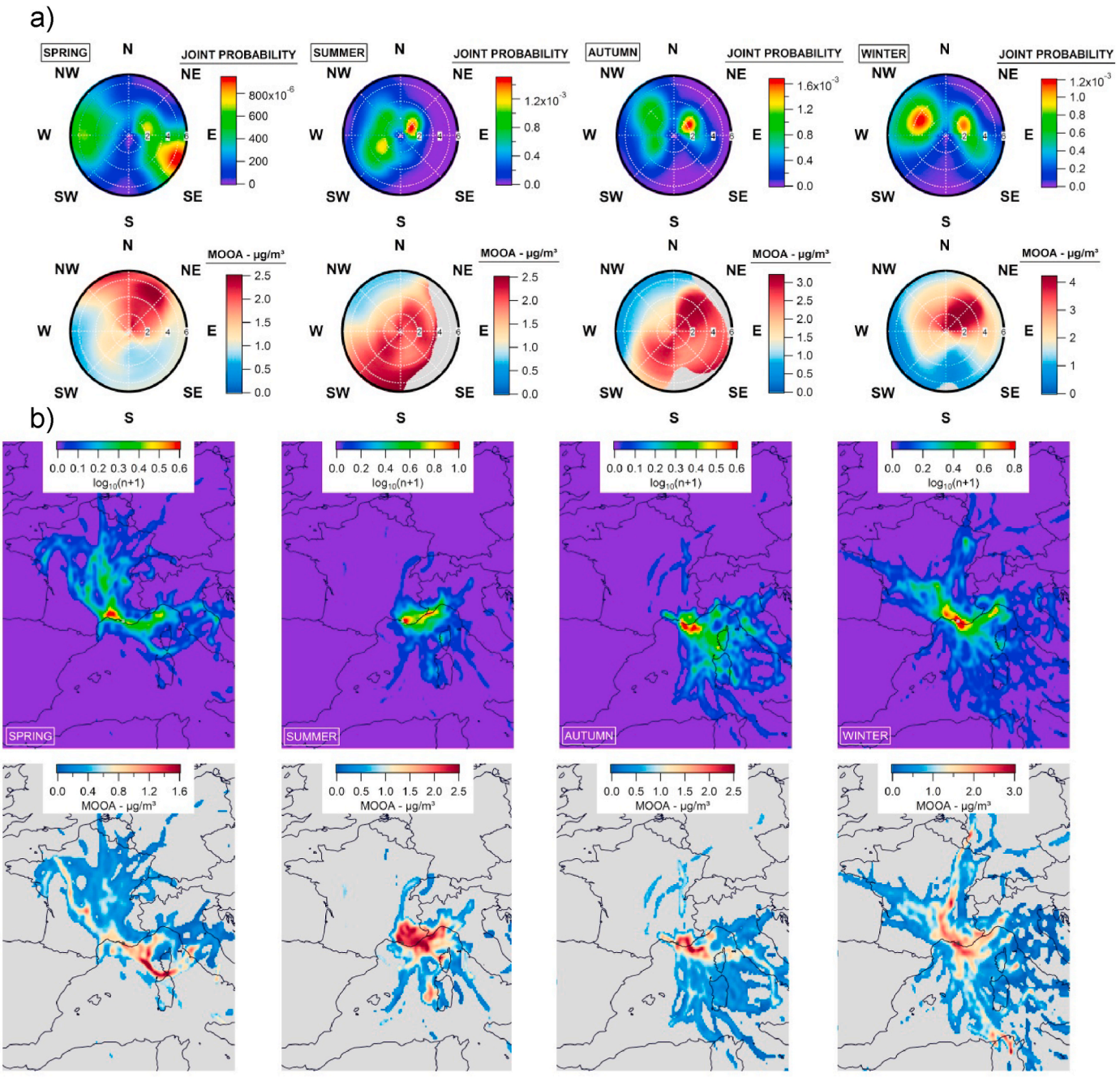

Fig. 8. (a) Seasonal wind roses (displayed as joint probability representing the wind frequency) and NWR plots for MOOA factor (in µg m^{-3}). Radial and tangential axes show respectively the wind speed ($m.s^{-1}$) and the wind direction (°). (b) Air masses occurrence for 72h-backtrajectories generated each 6 h and CWT maps for MOOA concentrations. The black dot endpoint represents the location of the MRS-LCP site.

The concentrations were associated with higher wind speeds than primary OA and LOOA PMF factors. While the north-east land breeze advected aged air masses back to the sampling site, enhanced concentrations were associated with southerly winds from the Mediterranean Sea (summer and autumn) and with the North sector with strong Mistral (spring).

Since wind components measured at MRS-LCP site are not necessary representative of the initial origin of air masses, MOOA concentrations were coupled with backtrajectories analysis. CWT calculations were performed (Fig. 8b) as they have already proved their ability to trace the geographical origin of long-range aerosol species (Petit et al., 2017a, 2019). To prevent for the local influence of wind recirculation (e.g. sea/land breezes cycle) data points linked to low speed conditions (<1 m s^{-1}) were filtered out. Based on these data, the spring CWT only accounted for 2018 period (March–April). Thus some high MOOA contributions were not represented here such as one of the main polluted episode from 14th to march 17, 2017 (Figure A17) which showed high concentrations of OA and ammonium nitrate attributed to the Rhône Valley region (Chazeau et al., 2021). For every season CWT analysis revealed eastern Mediterranean origin between the southern coast of France and the surroundings of Corsica Island. These hotspots can be assigned to natural as well as anthropogenic sources. Indeed highly oxidized OA measured during the PEACETIME oceanographic campaign accounted for up to 50% of organic fraction in sea spray aerosol in the west Mediterranean Sea (Freney et al., 2021), underlining the importance of OOA type aerosol in primary particles. In addition, the source

areas around Corsica might be associated to long-range and medium-lived anthropogenic VOCs highlighting potential sources such as shipping activity (Michoud et al., 2017). Unlike the oxygenated profile found for Sh-IndOA, the factor was determined from measured SO_2 concentrations and thus only prevailed for local ship emissions from Marseille harbour. MOOA could therefore involve an additional shipping contribution. In summer, MOOA concentrations are spread over the surrounding region (named "region Sud"). The focused trajectory density in the area may suggest warm and stagnant conditions which favoured local biogenic emissions from the vegetation and their low dispersion. In winter, CWT showed hotspots along the Rhône Valley. In this region, polluted air masses may be connected to known anthropogenic activities such as dense road traffic and industrial emissions from the "Chemical Valley". It has to be noted that some potential hotspot, such as the one located in central France in spring, might be falsely attributed to the related region due to the corridor effect (Michoud et al., 2017).

5. Summary and conclusion

The study presented the PMF source apportionment of OA measured with a ToF-ACSM from February 2017 to April 2018 (14 months) at the MRS-LCP site in Marseille. A novel approach was performed by applying PMF on a rolling window of 14 days using the new designed SoFi Pro. This method provided the decomposition of time dependant factor profiles which were more able to capture the OA sources variability through seasons compared to batch PMF analysis for the full dataset. However, it remained complex to model the OA composition with the rolling method during fast environmental changes. Some improvements are needed to deeply investigate these periods not well captured with a 14-days window and could require additional factors.

The a-value space for the applied PMF constraints was fully explored to determine the best OA sources separation. The PMF runs selection for the averaged solution was also improved based on a criteria selection, which consists in comparison with source external tracers or diurnal profile inspection. The final solution allowed to identify 5 to 6 factors throughout the year: 3 primary sources (HOA, COA and BBOA), 2 secondary sources (LOOA and MOOA), and a new oxygenated Sh-IndOA factor corresponding to the mixing industrial and shipping emissions. On average, the secondary OA fraction was predominant with 39.6% for MOOA and 21.5% for LOOA, followed by BBOA (11.7%), COA (11.5%), HOA (11.2%) and Sh-IndOA (4.5%). PMF uncertainty was assessed for each factor with satisfactory results of ±21%, ±24%, ±27%, ±34%, ±15% and ±31% for HOA, COA, Sh-IndOA, LOOA, MOOA and BBOA, respectively. Unlike the proximity of an extended industrial area and a large harbour expected to impact the city air pollution, Sh-IndOA source contribution to total OA remains low and seems to be more affiliated to UFPs and sulfate emissions. However, additional aged emissions from MOOA factor might account for the shipping activity over the Mediterranean Sea. While HOA and COA primary factor profiles were stable with constant contributions through the study period, BBOA was only present in winter, spring and half of autumn. This last factor accounted for different sources according to the seasons. First, a mass spectra profile assimilated to those of reference studies was attributed to domestic heating during the winter period. Then, a more aged profile showing decreasing f60 and increasing f44 due to oxygenated processes was accounted for the spring and autumn period and was linked to the surrounding land and agricultural waste burning. The secondary fraction represented 70% of the total OA in summer and was mainly attributed to biogenic activity from the enclosing vegetation. In winter, spring and autumn SOA concentrations may arise from oxidized combustion sources such as biomass burning or road traffic. Additionally, the more oxygenated SOA (MOOA) was partly driven by long-range transport with potential anthropogenic emissions from the Rhône valley (mostly in winter) and a strong origin from the west Mediterranean Sea (for every season).

This study emphasized the importance of dynamic factor profiles to assess the variability of long-term dataset, notably for the secondary origin. It would be necessary to apply the rolling method to more year-long ACSM datasets to corroborate its improved performances compared to the conventional seasonal PMF. Within the framework of these conclusions, the rolling approach constitutes a first step for automated analysis of continuous growing ACSM dataset.

Data availability

Data are available upon request to the contact author Benjamin Chazeau (Benjamin.chazeau@univ-amu.fr).

CRediT authorship contribution statement

Benjamin Chazeau: Formal analysis, Writing – original draft, contributed to the measurements. performed the analysis and wrote the paper. **Imad El Haddad:** Formal analysis, Writing – review & editing, and were involved in the source apportionment analysis and the interpretations. reviewed and all the authors commented on the paper. **Francesco Canonaco:** Formal analysis, Writing – review & editing, were involved in the source apportionment analysis and the interpretations. reviewed and all the authors commented on the paper. **Brice Temime-Roussel:** Writing – review & editing, and reviewed and all the authors commented on the paper. **Barbara D'Anna:** Writing – review & editing, reviewed and all the authors commented on the paper. **Grégory Gille:** and contributed to the measurements. **Boualem Mesbah:** contributed to the measurements. **André S.H. Prévôt:** Writing – review & editing, reviewed and all the authors commented on the paper. **Henri Wortham:** Writing – review & editing, reviewed and all the authors commented on the paper. **Nicolas Marchand:** Writing – review & editing, reviewed and all the authors commented on the paper, designed the research.

Declaration of competing interest

The authors declare that they have no known competing financial interests or personal relationships that could have appeared to influence the work reported in this paper.

Acknowledgements

This work is supported by AtmoSud, ANRT, the PACA Region and the French ministry of Environment. BC would also like to acknowledge the COST Action COLOSSAL (Chemical On-Line cOmpoSition and Source Apportionment of fine aerosol – CA16109).

Appendix A. Supplementary data

Supplementary data to this article can be found online at https://doi.org/10.1016/j.aeaoa.2022.100176.

References

Ahern, A.T., Robinson, E.S., Tkacik, D.S., Saleh, R., Hatch, L.E., Barsanti, K.C., Stockwell, C.E., Yokelson, R.J., Presto, A.A., Robinson, A.L., Sullivan, R.C., Donahue, N.M., 2019. Production of secondary organic aerosol during aging of biomass burning smoke from fresh fuels and its relationship to VOC precursors. J. Geophys. Res. Atmos. 124, 3583–3606. https://doi.org/10.1029/2018JD029068.

Alfarra, M.R., Hamilton, J.F., Wyche, K.P., Good, N., Ward, M.W., Carr, T., Barley, M.H., Monks, P.S., Jenkin, M.E., Lewis, A.C., McFiggans, G.B., 2012. The effect of photochemical ageing and initial precursor concentration on the composition and hygroscopic properties of β-caryophyllene secondary organic aerosol. Atmos. Chem. Phys. 12, 6417–6436. https://doi.org/10.5194/acp-12-6417-2012.

Alfarra, M.R., Prevot, A.S.H., Szidat, S., Sandradewi, J., Weimer, S., Lanz, V.A., Schreiber, D., Mohr, M., Baltensperger, U., 2007. Identification of the mass spectral signature of organic aerosols from wood burning emissions. Environ. Sci. Technol. 41, 5770–5777. https://doi.org/10.1021/es062289b.

Allan, J.D., Delia, A.E., Coe, H., Bower, K.N., Alfarra, M.R., Jimenez, J.L., Middlebrook, A.M., Drewnick, F., Onasch, T.B., Canagaratna, M.R., Jayne, J.T., Worsnop, D.R., 2004. A generalised method for the extraction of chemically resolved mass spectra from Aerodyne aerosol mass spectrometer data. J. Aerosol Sci. 35, 909–922. https://doi.org/10.1016/j.jaerosci.2004.02.007.

Ashbaugh, L.L., Malm, W.C., Sadeh, W.Z., 1985. A residence time probability analysis of sulfur concentrations at grand Canyon National Park. Atmos. Environ. 19, 1263–1270. https://doi.org/10.1016/0004-6981(85)90256-2, 1967.

Bozzetti, C., El Haddad, I., Salameh, D., Daellenbach, K.R., Fermo, P., Gonzalez, R., Minguillón, M.C., Iinuma, Y., Poulain, L., Elser, M., Müller, E., Slowik, J.G., Jaffrezo, J.-L., Baltensperger, U., Marchand, N., Prévôt, A.S.H., 2017a. Organic aerosol source apportionment by offline-AMS over a full year in Marseille. Atmos. Chem. Phys. 17, 8247–8268. https://doi.org/10.5194/acp-17-8247-2017.

Bozzetti, C., Sosedova, Y., Xiao, M., Daellenbach, K.R., Ulevicius, V., Dudoitis, V., Mordas, G., Byčenkienė, S., Plauškaitė, K., Vlachou, A., Golly, B., Chazeau, B., Besombes, J.-L., Baltensperger, U., Jaffrezo, J.-L., Slowik, J.G., El Haddad, I., Prévôt, A.S.H., 2017b. Argon offline-AMS source apportionment of organic aerosol over yearly cycles for an urban, rural, and marine site in northern Europe. Atmos. Chem. Phys. 17, 117–141. https://doi.org/10.5194/acp-17-117-2017.

Bressi, M., Cavalli, F., Belis, C.A., Putaud, J.-P., Fröhlich, R., Martins dos Santos, S., Petralia, E., Prévôt, A.S.H., Berico, M., Malaguti, A., Canonaco, F., 2016. Variations in the chemical composition of the submicron aerosol and in the sources of the organic fraction at a regional background site of the Po Valley (Italy). Atmos. Chem. Phys. 16, 12875–12896. https://doi.org/10.5194/acp-16-12875-2016.

Burtscher, H., 2005. Physical characterization of particulate emissions from diesel engines: a review. J. Aerosol Sci. 36, 896–932. https://doi.org/10.1016/j.jaerosci.2004.12.001.

Canagaratna, M.R., Jayne, J.T., Jimenez, J.L., Allan, J.D., Alfarra, M.R., Zhang, Q., Onasch, T.B., Drewnick, F., Coe, H., Middlebrook, A., Delia, A., Williams, L.R., Trimborn, A.M., Northway, M.J., DeCarlo, P.F., Kolb, C.E., Davidovits, P., Worsnop, D.R., 2007. Chemical and microphysical characterization of ambient aerosols with the aerodyne aerosol mass spectrometer. Mass Spectrom. Rev. 26, 185–222. https://doi.org/10.1002/mas.20115.

Canagaratna, M.R., Jimenez, J.L., Kroll, J.H., Chen, Q., Kessler, S.H., Massoli, P., Hildebrandt Ruiz, L., Fortner, E., Williams, L.R., Wilson, K.R., Surratt, J.D., Donahue, N.M., Jayne, J.T., Worsnop, D.R., 2015. Elemental ratio measurements of organic compounds using aerosol mass spectrometry: characterization, improved calibration, and implications. Atmos. Chem. Phys. 15, 253–272. https://doi.org/10.5194/acp-15-253-2015.

Canonaco, F., Crippa, M., Slowik, J.G., Baltensperger, U., Prévôt, A.S.H., 2013. SoFi, an IGOR-based interface for the efficient use of the generalized multilinear engine (ME-2) for the source apportionment: ME-2 application to aerosol mass spectrometer data. Atmos. Meas. Tech. 6, 3649–3661. https://doi.org/10.5194/amt-6-3649-2013.

Canonaco, F., Slowik, J.G., Baltensperger, U., Prévôt, A.S.H., 2015. Seasonal differences in oxygenated organic aerosol composition: implications for emissions sources and factor analysis. Atmos. Chem. Phys. 15, 6993–7002. https://doi.org/10.5194/acp-15-6993-2015.

Canonaco, F., Tobler, A., Chen, G., Sosedova, Y., Slowik, J.G., Bozzetti, C., Daellenbach, K.R., El Haddad, I., Crippa, M., Huang, R.-J., Furger, M., Baltensperger, U., Prévôt, A.S.H., 2021. A new method for long-term source apportionment with time-dependent factor profiles and uncertainty assessment using SoFi Pro: application to 1 year of organic aerosol data. Atmos. Meas. Tech. 14, 923–943. https://doi.org/10.5194/amt-14-923-2021.

Chazeau, B., Temime-Roussel, B., Gille, G., Mesbah, B., D'Anna, B., Wortham, H., Marchand, N., 2021. Measurement report: fourteen months of real-time characterisation of the submicronic aerosol and its atmospheric dynamics at the Marseille–Longchamp supersite. Atmos. Chem. Phys. 21, 7293–7319. https://doi.org/10.5194/acp-21-7293-2021.

Chen, G., Sosedova, Y., Canonaco, F., Fröhlich, R., Tobler, A., Vlachou, A., Daellenbach, K.R., Bozzetti, C., Hueglin, C., Graf, P., Baltensperger, U., Slowik, J.G., El Haddad, I., Prévôt, A.S.H., 2021. Time-dependent source apportionment of submicron organic aerosol for a rural site in an alpine valley using a rolling positive matrix factorisation (PMF) window. Atmos. Chem. Phys. 21, 15081–15101. https://doi.org/10.5194/acp-21-15081-2021.

Chirico, R., Prevot, A.S.H., DeCarlo, P.F., Heringa, M.F., Richter, R., Weingartner, E., Baltensperger, U., 2011. Aerosol and trace gas vehicle emission factors measured in a tunnel using an Aerosol Mass Spectrometer and other on-line instrumentation. Atmos. Environ. 45, 2182–2192. https://doi.org/10.1016/j.atmosenv.2011.01.069.

Clapp, L., 2001. Analysis of the relationship between ambient levels of O3, NO2 and NO as a function of NOx in the UK. Atmos. Environ. 35, 6391–6405. https://doi.org/10.1016/S1352-2310(01)00378-8.

Cohen, A.J., Brauer, M., Burnett, R., Anderson, H.R., Frostad, J., Estep, K., Balakrishnan, K., Brunekreef, B., Dandona, L., Dandona, R., Feigin, V., Freedman, G., Hubbell, B., Jobling, A., Kan, H., Knibbs, L., Liu, Y., Martin, R., Morawska, L., Pope, C.A., Shin, H., Straif, K., Shaddick, G., Thomas, M., van Dingenen, R., van Donkelaar, A., Vos, T., Murray, C.J.L., Forouzanfar, M.H., 2017. Estimates and 25-year trends of the global burden of disease attributable to ambient air pollution: an analysis of data from the Global Burden of Diseases Study 2015. Lancet 389, 1907–1918. https://doi.org/10.1016/S0140-6736(17)30505-6.

Coudray, N., Dieterlen, A., Roth, E., Trouvé, G., 2009. Density measurement of fine aerosol fractions from wood combustion sources using ELPI distributions and image processing techniques. Fuel 88, 947–954. https://doi.org/10.1016/j.fuel.2008.12.013.

Crippa, M., Canonaco, F., Lanz, V.A., Äijälä, M., Allan, J.D., Carbone, S., Capes, G., Ceburnis, D., Dall'Osto, M., Day, D.A., DeCarlo, P.F., Ehn, M., Eriksson, A., Freney, E., Hildebrandt Ruiz, L., Hillamo, R., Jimenez, J.L., Junninen, H., Kiendler-Scharr, A., Kortelainen, A.-M., Kulmala, M., Laaksonen, A., Mensah, A.A., Mohr, C., Nemitz, E., O'Dowd, C., Ovadnevaite, J., Pandis, S.N., Petäjä, T., Poulain, L., Saarikoski, S., Sellegri, K., Swietlicki, E., Tiitta, P., Worsnop, D.R., Baltensperger, U., Prévôt, A.S.H., 2014. Organic aerosol components derived from 25 AMS data sets across Europe using a consistent ME-2 based source apportionment approach. Atmos. Chem. Phys. 14, 6159–6176. https://doi.org/10.5194/acp-14-6159-2014.

Crippa, M., DeCarlo, P.F., Slowik, J.G., Mohr, C., Heringa, M.F., Chirico, R., Poulain, L., Freutel, F., Sciare, J., Cozic, J., Di Marco, C.F., Elsasser, M., Nicolas, J.B., Marchand, N., Abidi, E., Wiedensohler, A., Drewnick, F., Schneider, J., Borrmann, S., Nemitz, E., Zimmermann, R., Jaffrezo, J.-L., Prévôt, A.S.H., Baltensperger, U., 2013. Wintertime aerosol chemical composition and source apportionment of the organic fraction in the metropolitan area of Paris. Atmos. Chem. Phys. 13, 961–981. https://doi.org/10.5194/acp-13-961-2013.

Cubison, M.J., Ortega, A.M., Hayes, P.L., Farmer, D.K., Day, D., Lechner, M.J., Brune, W. H., Apel, E., Diskin, G.S., Fisher, J.A., Fuelberg, H.E., Hecobian, A., Knapp, D.J., Mikoviny, T., Riemer, D., Sachse, G.W., Sessions, W., Weber, R.J., Weinheimer, A.J., Wisthaler, A., Jimenez, J.L., 2011. Effects of aging on organic aerosol from open biomass burning smoke in aircraft and laboratory studies. Atmos. Chem. Phys. 11, 12049–12064. https://doi.org/10.5194/acp-11-12049-2011.

Daellenbach, K.R., Bozzetti, C., Křepelová, A., Canonaco, F., Wolf, R., Zotter, P., Fermo, P., Crippa, M., Slowik, J.G., Sosedova, Y., Zhang, Y., Huang, R.-J., Poulain, L., Szidat, S., Baltensperger, U., El Haddad, I., Prévôt, A.S.H., 2016. Characterization and source apportionment of organic aerosol using offline aerosol mass spectrometry. Atmos. Meas. Tech. 9, 23–39. https://doi.org/10.5194/amt-9-23-2016.

Daellenbach, K.R., Stefenelli, G., Bozzetti, C., Vlachou, A., Fermo, P., Gonzalez, R., Piazzalunga, A., Colombi, C., Canonaco, F., Hueglin, C., Kasper-Giebl, A., Jaffrezo, J.-L., Bianchi, F., Slowik, J.G., Baltensperger, U., El-Haddad, I., Prévôt, A.S. H., 2017. Long-term chemical analysis and organic aerosol source apportionment at nine sites in central Europe: source identification and uncertainty assessment. Atmos. Chem. Phys. 17, 13265–13282. https://doi.org/10.5194/acp-17-13265-2017.

Daellenbach, K.R., Uzu, G., Jiang, J., Cassagnes, L.-E., Leni, Z., Vlachou, A., Stefenelli, G., Canonaco, F., Weber, S., Segers, A., Kuenen, J.J.P., Schaap, M., Favez, O., Albinet, A., Aksoyoglu, S., Dommen, J., Baltensperger, U., Geiser, M., El Haddad, I., Jaffrezo, J.-L., Prévôt, A.S.H., 2020. Sources of particulate-matter air pollution and its oxidative potential in Europe. Nature 587, 20. https://doi.org/10.1038/s41586-020-2902-8.

Debevec, C., Sauvage, S., Gros, V., Sciare, J., Pikridas, M., Stavroulas, I., Salameh, T., Leonardis, T., Gaudion, V., Depelchin, L., Fronval, I., Sarda-Esteve, R., Baisnée, D., Bonsang, B., Savvides, C., Vrekoussis, M., Locoge, N., 2017. Origin and variability in volatile organic compounds observed at an Eastern Mediterranean background site (Cyprus). Atmos. Chem. Phys. 17, 11355–11388. https://doi.org/10.5194/acp-17-11355-2017.

Drinovec, L., Močnik, G., Zotter, P., Prévôt, A.S.H., Ruckstuhl, C., Coz, E., Rupakheti, M., Sciare, J., Müller, T., Wiedensohler, A., Hansen, A.D.A., 2015. The "dual-spot" Aethalometer: an improved measurement of aerosol black carbon with real-time loading compensation. Atmos. Meas. Tech. 8, 1965–1979. https://doi.org/10.5194/amt-8-1965-2015.

Dzepina, K., Arey, J., Marr, L.C., Worsnop, D.R., Salcedo, D., Zhang, Q., Onasch, T.B., Molina, L.T., Molina, M.J., Jimenez, J.L., 2007. Detection of particle-phase polycyclic aromatic hydrocarbons in Mexico City using an aerosol mass spectrometer. Int. J. Mass Spectrom. 263, 152–170. https://doi.org/10.1016/j.ijms.2007.01.010.

Efron, B., 1979. Bootstrap methods: another look at the jackknife. Ann. Stat. 7, 1–26.

El Haddad, I., D'Anna, B., Temime-Roussel, B., Nicolas, M., Boreave, A., Favez, O., Voisin, D., Sciare, J., George, C., Jaffrezo, J.-L., Wortham, H., Marchand, N., 2013. Towards a better understanding of the origins, chemical composition and aging of oxygenated organic aerosols: case study of a Mediterranean industrialized environment, Marseille. Atmos. Chem. Phys. 13, 7875–7894. https://doi.org/10.5194/acp-13-7875-2013.

El Haddad, I., Marchand, N., Temime-Roussel, B., Wortham, H., Piot, C., Besombes, J.-L., Baduel, C., Voisin, D., Armengaud, A., Jaffrezo, J.-L., 2011a. Insights into the secondary fraction of the organic aerosol in a Mediterranean urban area: Marseille. Atmos. Chem. Phys. 11, 2059–2079. https://doi.org/10.5194/acp-11-2059-2011.

El Haddad, I., Marchand, N., Wortham, H., Piot, C., Besombes, J.-L., Cozic, J., Chauvel, C., Armengaud, A., Robin, D., Jaffrezo, J.-L., 2011b. Primary sources of PM2.5 organic aerosol in an industrial Mediterranean city, Marseille. Atmos. Chem. Phys. 11, 2039–2058. https://doi.org/10.5194/acp-11-2039-2011.

Elser, M., Huang, R.-J., Wolf, R., Slowik, J.G., Wang, Q., Canonaco, F., Li, G., Bozzetti, C., Daellenbach, K.R., Huang, Y., Zhang, R., Li, Z., Cao, J., Baltensperger, U., El-Haddad, I., Prévôt, A.S.H., 2016. New insights into PM2.5 chemical composition and sources in two major cities in China during extreme haze events using aerosol mass spectrometry. Atmos. Chem. Phys. 16, 3207–3225. https://doi.org/10.5194/acp-16-3207-2016.

Farmer, D.K., Matsunaga, A., Docherty, K.S., Surratt, J.D., Seinfeld, J.H., Ziemann, P.J., Jimenez, J.L., 2010. Response of an aerosol mass spectrometer to organonitrates and organosulfates and implications for atmospheric chemistry. Proc. Natl. Acad. Sci. Unit. States Am. 107, 6670–6675. https://doi.org/10.1073/pnas.0912340107.

Favez, O., El Haddad, I., Piot, C., Boréave, A., Abidi, E., Marchand, N., Jaffrezo, J.-L., Besombes, J.-L., Personnaz, M.-B., Sciare, J., Wortham, H., George, C., D'Anna, B., 2010. Inter-comparison of source apportionment models for the estimation of wood burning aerosols during wintertime in an Alpine city (Grenoble, France). Atmos. Chem. Phys. 10, 5295–5314. https://doi.org/10.5194/acp-10-5295-2010.

Fountoukis, C., Megaritis, A.G., Skyllakou, K., Charalampidis, P.E., Pilinis, C., Denier van der Gon, H.A.C., Crippa, M., Canonaco, F., Mohr, C., Prévôt, A.S.H., Allan, J.D.,

Poulain, L., Petäjä, T., Tiitta, P., Carbone, S., Kiendler-Scharr, A., Nemitz, E., O& apos, Dowd, C., Swietlicki, E., Pandis, S.N., 2014. Organic aerosol concentration and composition over Europe: insights from comparison of regional model predictions with aerosol mass spectrometer factor analysis. Atmos. Chem. Phys. 14, 9061–9076. https://doi.org/10.5194/acp-14-9061-2014.

Freney, E., Sellegri, K., Nicosia, A., Williams, L.R., Rinaldi, M., Trueblood, J.T., Prévôt, A. S.H., Thyssen, M., Grégori, G., Haëntjens, N., Dinasquet, J., Obernosterer, I., Van Wambeke, F., Engel, A., Zäncker, B., Desboeufs, K., Asmi, E., Timonen, H., Guieu, C., 2021. Mediterranean nascent sea spray organic aerosol and relationships with seawater biogeochemistry. Atmos. Chem. Phys. 21, 10625–10641. https://doi.org/10.5194/acp-21-10625-2021.

Freney, E.J., Sellegri, K., Canonaco, F., Boulon, J., Hervo, M., Weigel, R., Pichon, J.M., Colomb, A., Prévôt, A.S.H., Laj, P., 2011. Seasonal variations in aerosol particle composition at the puy-de-Dôme research station in France. Atmos. Chem. Phys. 11, 13047–13059. https://doi.org/10.5194/acp-11-13047-2011.

Fröhlich, R., Crenn, V., Setyan, A., Belis, C.A., Canonaco, F., Favez, O., Riffault, V., Slowik, J.G., Aas, W., Aijälä, M., Alastuey, A., Artiñano, B., Bonnaire, N., Bozzetti, C., Bressi, M., Carbone, C., Coz, E., Croteau, P.L., Cubison, M.J., Esser-Gietl, J.K., Green, D.C., Gros, V., Heikkinen, L., Herrmann, H., Jayne, J.T., Lunder, C.R., Minguillón, M.C., Močnik, G., O'Dowd, C.D., Ovadnevaite, J., Petralia, E., Poulain, L., Priestman, M., Ripoll, A., Sarda-Estève, R., Wiedensohler, A., Baltensperger, U., Sciare, J., Prévôt, A.S.H., 2015a. ACTRIS ACSM intercomparison – Part 2: intercomparison of ME-2 organic source apportionment results from 15 individual, co-located aerosol mass spectrometers. Atmos. Meas. Tech. 8, 2555–2576. https://doi.org/10.5194/amt-8-2555-2015.

Fröhlich, R., Cubison, M.J., Slowik, J.G., Bukowiecki, N., Canonaco, F., Croteau, P.L., Gysel, M., Henne, S., Herrmann, E., Jayne, J.T., Steinbacher, M., Worsnop, D.R., Baltensperger, U., Prévôt, A.S.H., 2015b. Fourteen months of on-line measurements of the non-refractory submicron aerosol at the Jungfraujoch (3580 m a.s.l.) – chemical composition, origins and organic aerosol sources. Atmos. Chem. Phys. 15, 11373–11398. https://doi.org/10.5194/acp-15-11373-2015.

Fröhlich, R., Cubison, M.J., Slowik, J.G., Bukowiecki, N., Prévôt, A.S.H., Baltensperger, U., Schneider, J., Kimmel, J.R., Gonin, M., Rohner, U., Worsnop, D.R., Jayne, J.T., 2013. The ToF-ACSM: a portable aerosol chemical speciation monitor with TOFMS detection. Atmos. Meas. Tech. 6, 3225–3241. https://doi.org/10.5194/amt-6-3225-2013.

Fry, J.L., Draper, D.C., Zarzana, K.J., Campuzano-Jost, P., Day, D.A., Jimenez, J.L., Brown, S.S., Cohen, R.C., Kaser, L., Hansel, A., Cappellin, L., Karl, T., Hodzic Roux, A., Turnipseed, A., Cantrell, C., Lefer, B.L., Grossberg, N., 2013. Observations of gas- and aerosol-phase organic nitrates at BEACHON-RoMBAS 2011. Atmos. Chem. Phys. 13, 8585–8605. https://doi.org/10.5194/acp-13-8585-2013.

González, Y., Rodríguez, S., Guerra García, J.C., Trujillo, J.L., García, R., 2011. Ultrafine particles pollution in urban coastal air due to ship emissions. Atmos. Environ. 45, 4907–4914. https://doi.org/10.1016/j.atmosenv.2011.06.002.

Heikkinen, L., Äijälä, M., Riva, M., Luoma, K., Dällenbach, K., Aalto, J., Aalto, P., Aliaga, D., Aurela, M., Keskinen, H., Makkonen, U., Rantala, P., Kulmala, M., Petäjä, T., Worsnop, D., Ehn, M., 2020. Long-term sub-micrometer aerosol chemical composition in the boreal forest: inter- and intra-annual variability. Atmos. Chem. Phys. 20, 3151–3180. https://doi.org/10.5194/acp-20-3151-2020.

Hennigan, C.J., Miracolo, M.A., Engelhart, G.J., May, A.A., Presto, A.A., Lee, T., Sullivan, A.P., McMeeking, G.R., Coe, H., Wold, C.E., Hao, W.-M., Gilman, J.B., Kuster, W.C., de Gouw, J., Schichtel, B.A., Collett, J.L., Kreidenweis, S.M., Robinson, A.L., 2011. Chemical and physical transformations of organic aerosol from the photo-oxidation of open biomass burning emissions in an environmental chamber. Atmos. Chem. Phys. 11, 7669–7686. https://doi.org/10.5194/acp-11-7669-2011.

Hennigan, C.J., Sullivan, A.P., Collett, J.L., Robinson, A.L., 2010. Levoglucosan stability in biomass burning particles exposed to hydroxyl radicals: levoglucosan stability IN aerosol. Geophys. Res. Lett. 37 https://doi.org/10.1029/2010GL043088 n, /a-n/a.

Henry, R., Norris, G.A., Vedantham, R., Turner, J.R., 2009. Source region identification using kernel smoothing. Environ. Sci. Technol. 43, 4090–4097. https://doi.org/10.1021/es8011723.

Heringa, M.F., DeCarlo, P.F., Chirico, R., Tritscher, T., Dommen, J., Weingartner, E., Richter, R., Wehrle, G., Prévôt, A.S.H., Baltensperger, U., 2011. Investigations of primary and secondary particulate matter of different wood combustion appliances with a high-resolution time-of-flight aerosol mass spectrometer. Atmos. Chem. Phys. 11, 5945–5957. https://doi.org/10.5194/acp-11-5945-2011.

Jayne, J.T., Leard, D.C., Zhang, X., Davidovits, P., Smith, K.A., Kolb, C.E., Worsnop, D.R., 2000. Development of an aerosol mass spectrometer for size and composition analysis of submicron particles. Aerosol. Sci. Technol. 33, 49–70. https://doi.org/10.1080/027868200410840.

Jimenez, J.L., Canagaratna, M.R., Donahue, N.M., Prevot, A.S.H., Zhang, Q., Kroll, J.H., DeCarlo, P.F., Allan, J.D., Coe, H., Ng, N.L., Aiken, A.C., Docherty, K.S., Ulbrich, I. M., Grieshop, A.P., Robinson, A.L., Duplissy, J., Smith, J.D., Wilson, K.R., Lanz, V.A., Hueglin, C., Sun, Y.L., Tian, J., Laaksonen, A., Raatikainen, T., Rautiainen, J., Vaattovaara, P., Ehn, M., Kulmala, M., Tomlinson, J.M., Collins, D.R., Cubison, M.J. E., Dunlea, J., Huffman, J.A., Onasch, T.B., Alfarra, M.R., Williams, P.I., Bower, K., Kondo, Y., Schneider, J., Drewnick, F., Borrmann, S., Weimer, S., Demerjian, K., Salcedo, D., Cottrell, L., Griffin, R., Takami, A., Miyoshi, T., Hatakeyama, S., Shimono, A., Sun, J.Y., Zhang, Y.M., Dzepina, K., Kimmel, J.R., Sueper, D., Jayne, J. T., Herndon, S.C., Trimborn, A.M., Williams, L.R., Wood, E.C., Middlebrook, A.M., Kolb, C.E., Baltensperger, U., Worsnop, D.R., 2009. Evolution of organic aerosols in the atmosphere. Science 326, 1525–1529. https://doi.org/10.1126/science.1180353.

Kiendler-Scharr, A., Mensah, A.A., Friese, E., Topping, D., Nemitz, E., Prevot, A.S.H., Äijälä, M., Allan, J., Canonaco, F., Canagaratna, M., Carbone, S., Crippa, M., Dall Osto, M., Day, D.A., De Carlo, P., Di Marco, C.F., Elbern, H., Eriksson, A., Freney, E., Hao, L., Herrmann, H., Hildebrandt, L., Hillamo, R., Jimenez, J.L., Laaksonen, A., McFiggans, G., Mohr, C., O'Dowd, C., Otjes, R., Ovadnevaite, J., Pandis, S.N., Poulain, L., Schlag, P., Sellegri, K., Swietlicki, E., Tiitta, P., Vermeulen, A., Wahner, A., Worsnop, D., Wu, H.-C., 2016. Ubiquity of organic nitrates from nighttime chemistry in the European submicron aerosol: organic Nitrates in European PM1. Geophys. Res. Lett. 43, 7735–7744. https://doi.org/10.1002/2016GL069239.

Kreyling, W.G., Semmler-Behnke, M., Möller, W., 2006. Ultrafine particle–lung interactions: does size matter? J. Aerosol Med. 19, 74–83. https://doi.org/10.1089/jam.2006.19.74.

Lanz, V.A., Alfarra, M.R., Baltensperger, U., Buchmann, B., Hueglin, C., Prévôt, A.S.H., 2007. Source apportionment of submicron organic aerosols at an urban site by factor analytical modelling of aerosol mass spectra. Atmos. Chem. Phys. 7, 1503–1522. https://doi.org/10.5194/acp-7-1503-2007.

Lanz, V.A., Alfarra, M.R., Baltensperger, U., Buchmann, B., Hueglin, C., Szidat, S., Wehrli, M.N., Wacker, L., Weimer, S., Caseiro, A., Puxbaum, H., Prevot, A.S.H., 2008. Source attribution of submicron organic aerosols during wintertime inversions by advanced factor Analysis of aerosol mass spectra. Environ. Sci. Technol. 42, 214–220. https://doi.org/10.1021/es0707207.

Lelieveld, J., Evans, J.S., Fnais, M., Giannadaki, D., Pozzer, A., 2015. The contribution of outdoor air pollution sources to premature mortality on a global scale. Nature 525, 367–371. https://doi.org/10.1038/nature15371.

Michoud, V., Sciare, J., Sauvage, S., Dusanter, S., Léonardis, T., Gros, V., Kalogridis, C., Zannoni, N., Féron, A., Petit, J.-E., Crenn, V., Baisnée, D., Sarda-Estève, R., Bonnaire, N., Marchand, N., DeWitt, H.L., Pey, J., Colomb, A., Gheusi, F., Szidat, S., Stavroulas, I., Borbon, A., Locoge, N., 2017. Organic carbon at a remote site of the western Mediterranean Basin: sources and chemistry during the ChArMEx SOP2 field experiment. Atmos. Chem. Phys. 17, 8837–8865. https://doi.org/10.5194/acp-17-8837-2017.

Middlebrook, A.M., Bahreini, R., Jimenez, J.L., Canagaratna, M.R., 2012. Evaluation of composition-dependent collection efficiencies for the aerodyne aerosol mass spectrometer using field data. Aerosol. Sci. Technol. 46, 258–271. https://doi.org/10.1080/02786826.2011.620041.

Minguillón, M.C., Ripoll, A., Pérez, N., Prévôt, A.S.H., Canonaco, F., Querol, X., Alastuey, A., 2015. Chemical characterization of submicron regional background aerosols in the western Mediterranean using an Aerosol Chemical Speciation Monitor. Atmos. Chem. Phys. 15, 6379–6391. https://doi.org/10.5194/acp-15-6379-2015.

Mohr, C., DeCarlo, P.F., Heringa, M.F., Chirico, R., Slowik, J.G., Richter, R., Reche, C., Alastuey, A., Querol, X., Seco, R., Peñuelas, J., Jiménez, J.L., Crippa, M., Zimmermann, R., Baltensperger, U., Prévôt, A.S.H., 2012. Identification and quantification of organic aerosol from cooking and other sources in Barcelona using aerosol mass spectrometer data. Atmos. Chem. Phys. 12, 1649–1665. https://doi.org/10.5194/acp-12-1649-2012.

Ng, N.L., Canagaratna, M.R., Jimenez, J.L., Zhang, Q., Ulbrich, I.M., Worsnop, D.R., 2011a. Real-time methods for estimating organic component mass concentrations from aerosol mass spectrometer data. Environ. Sci. Technol. 45, 910–916. https://doi.org/10.1021/es102951k.

Ng, N.L., Canagaratna, M.R., Zhang, Q., Jimenez, J.L., Tian, J., Ulbrich, I.M., Kroll, J.H., Docherty, K.S., Chhabra, P.S., Bahreini, R., Murphy, S.M., Seinfeld, J.H., Hildebrandt, L., Donahue, N.M., DeCarlo, P.F., Lanz, V.A., Prévôt, A.S.H., Dinar, E., Rudich, Y., Worsnop, D.R., 2010. Organic aerosol components observed in northern hemispheric datasets from aerosol mass spectrometry. Atmos. Chem. Phys. 10, 4625–4641. https://doi.org/10.5194/acp-10-4625-2010.

Ng, N.L., Herndon, S.C., Trimborn, A., Canagaratna, M.R., Croteau, P.L., Onasch, T.B., Sueper, D., Worsnop, D.R., Zhang, Q., Sun, Y.L., Jayne, J.T., 2011b. An aerosol chemical speciation monitor (ACSM) for routine monitoring of the composition and mass concentrations of ambient aerosol. Aerosol. Sci. Technol. 45, 780–794. https://doi.org/10.1080/02786826.2011.560211.

Oberdörster, G., Sharp, Z., Atudorei, V., Elder, A., Gelein, R., Kreyling, W., Cox, C., 2004. Translocation of inhaled ultrafine particles to the brain. Inhal. Toxicol. 16, 437–445. https://doi.org/10.1080/08958370490439597.

Ovadnevaite, J., Ceburnis, D., Leinert, S., Dall'Osto, M., Canagaratna, M., O'Doherty, S., Berresheim, H., O'Dowd, C., 2014. Submicron NE Atlantic marine aerosol chemical composition and abundance: seasonal trends and air mass categorization: seasonal Trends of Marine Aerosol. J. Geophys. Res. Atmos. 119 (11), 850. https://doi.org/10.1002/2013JD021330, 11,863.

Paatero, P., 1999. The multilinear engine—a table-driven, least squares program for solving multilinear problems, including the n-way parallel factor Analysis model. J. Comput. Graph Stat. 8, 854–888. https://doi.org/10.1080/10618600.1999.10474853.

Paatero, P., Hopke, P.K., 2003. Discarding or downweighting high-noise variables in factor analytic models. Anal. Chim. Acta 490, 277–289. https://doi.org/10.1016/S0003-2670(02)01643-4.

Paatero, P., Tapper, U., 1994. Positive matrix factorization: a non-negative factor model with optimal utilization of error estimates of data values. Environmetrics 5, 111–126. https://doi.org/10.1002/env.3170050203.

Parra, R., Gassó, S., Baldasano, J.M., 2004. Estimating the biogenic emissions of non-methane volatile organic compounds from the North Western Mediterranean vegetation of Catalonia, Spain. Sci. Total Environ. 329, 241–259. https://doi.org/10.1016/j.scitotenv.2004.03.005.

Parworth, C., Fast, J., Mei, F., Shippert, T., Sivaraman, C., Tilp, A., Watson, T., Zhang, Q., 2015. Long-term measurements of submicrometer aerosol chemistry at the southern great plains (SGP) using an aerosol chemical speciation monitor (ACSM). Atmos. Environ. 106, 43–55. https://doi.org/10.1016/j.atmosenv.2015.01.060.

Petit, J.-E., Amodeo, T., Meleux, F., Bessagnet, B., Menut, L., Grenier, D., Pellan, Y., Ockler, A., Rocq, B., Gros, V., Sciare, J., Favez, O., 2017a. Characterising an intense PM pollution episode in March 2015 in France from multi-site approach and near real time data: climatology, variabilities, geographical origins and model evaluation. Atmos. Environ. 155, 68–84. https://doi.org/10.1016/j.atmosenv.2017.02.012.

Petit, J.-E., Favez, O., Albinet, A., Canonaco, F., 2017b. A user-friendly tool for comprehensive evaluation of the geographical origins of atmospheric pollution: wind and trajectory analyses. Environ. Model. Software 88, 183–187. https://doi.org/10.1016/j.envsoft.2016.11.022.

Petit, J.-E., Pallarès, C., Favez, O., Alleman, L.Y., Bonnaire, N., Rivière, E., 2019. Sources and geographical origins of PM10 in metz (France) using oxalate as a marker of secondary organic aerosols by positive matrix factorization analysis. Atmosphere 10, 370. https://doi.org/10.3390/atmos10070370.

Pfaffenberger, L., Barmet, P., Slowik, J.G., Praplan, A.P., Dommen, J., Prévôt, A.S.H., Baltensperger, U., 2013. The link between organic aerosol mass loading and degree of oxygenation: an α-pinene photooxidation study. Atmos. Chem. Phys. 13, 6493–6506. https://doi.org/10.5194/acp-13-6493-2013.

Pieber, S.M., El Haddad, I., Slowik, J.G., Canagaratna, M.R., Jayne, J.T., Platt, S.M., Bozzetti, C., Daellenbach, K.R., Fröhlich, R., Vlachou, A., Klein, F., Dommen, J., Miljevic, B., Jiménez, J.L., Worsnop, D.R., Baltensperger, U., Prévôt, A.S.H., 2016. Inorganic salt interference on CO2+ in aerodyne AMS and ACSM organic aerosol composition studies. Environ. Sci. Technol. 50, 10494–10503. https://doi.org/10.1021/acs.est.6b01035.

Pope, C.A., Burnett, R.T., Thun, M.J., Calle, E.E., Krewski, D., Ito, K., Thurston, G.D., 2002. Lung cancer, cardiopulmonary mortality, and long-term exposure to fine particulate air pollution. JAMA 287, 1132. https://doi.org/10.1001/jama.287.9.1132.

Pope, C.A., Dockery, D.W., 2006. Health effects of fine particulate air pollution: lines that connect. J. Air Waste Manag. Assoc. 56, 709–742. https://doi.org/10.1080/10473289.2006.10464485.

Reid, J.S., Koppmann, R., Eck, T.F., Eleuterio, D.P., 2005. A review of biomass burning emissions part II: intensive physical properties of biomass burning particles. Atmos. Chem. Phys. 27.

Reyes-Villegas, E., Green, D.C., Priestman, M., Canonaco, F., Coe, H., Prévôt, A.S.H., Allan, J.D., 2016. Organic aerosol source apportionment in London 2013 with ME-2: exploring the solution space with annual and seasonal analysis. Atmos. Chem. Phys. 16, 15545–15559. https://doi.org/10.5194/acp-16-15545-2016.

Ripoll, A., Minguillón, M.C., Pey, J., Jimenez, J.L., Day, D.A., Sosedova, Y., Canonaco, F., Prévôt, A.S.H., Querol, X., Alastuey, A., 2015. Long-term real-time chemical characterization of submicron aerosols at Montsec (southern Pyrenees, 1570 m a.s.l.). Atmos. Chem. Phys. 15, 2935–2951. https://doi.org/10.5194/acp-15-2935-2015.

Rodríguez, S., Cuevas, E., 2007. The contributions of “minimum primary emissions” and “new particle formation enhancements” to the particle number concentration in urban air. J. Aerosol Sci. 38, 1207–1219. https://doi.org/10.1016/j.jaerosci.2007.09.001.

Salameh, D., Pey, J., Bozzetti, C., El Haddad, I., Detournay, A., Sylvestre, A., Canonaco, F., Armengaud, A., Piga, D., Robin, D., Prevot, A.S.H., Jaffrezo, J.-L., Wortham, H., Marchand, N., 2018. Sources of PM2.5 at an urban-industrial Mediterranean city, Marseille (France): application of the ME-2 solver to inorganic and organic markers. Atmos. Res. 214, 263–274. https://doi.org/10.1016/j.atmosres.2018.08.005.

Sandradewi, J., Prévôt, A.S.H., Szidat, S., Perron, N., Alfarra, M.R., Lanz, V.A., Weingartner, E., Baltensperger, U., 2008. Using aerosol light absorption measurements for the quantitative determination of wood burning and traffic emission contributions to particulate matter. Environ. Sci. Technol. 42, 3316–3323. https://doi.org/10.1021/es702253m.

Schlag, P., Kiendler-Scharr, A., Blom, M.J., Canonaco, F., Henzing, J.S., Moerman, M., Prévôt, A.S.H., Holzinger, R., 2016. Aerosol source apportionment from 1-year measurements at the CESAR towerin Cabauw, The Netherlands. Atmos. Chem. Phys. 16, 8831–8847. https://doi.org/10.5194/acp-16-8831-2016.

Sciare, J., Oikonomou, K., Cachier, H., Mihalopoulos, N., Andreae, M.O., Maenhaut, W., Sarda-Estève, R., 2005. Aerosol mass closure and reconstruction of the light scattering coefficient over the Eastern Mediterranean Sea during the MINOS campaign. Atmos. Chem. Phys. 14.

Stavroulas, I., Bougiatioti, A., Grivas, G., Paraskevopoulou, D., Tsagkaraki, M., Zarmpas, P., Liakakou, E., Gerasopoulos, E., Mihalopoulos, N., 2019. Sources and processes that control the submicron organic aerosol composition in an urban Mediterranean environment (Athens): a high temporal-resolution chemical composition measurement study. Atmos. Chem. Phys. 19, 901–919. https://doi.org/10.5194/acp-19-901-2019.

Stein, A.F., Draxler, R.R., Rolph, G.D., Stunder, B.J.B., Cohen, M.D., Ngan, F., 2015. NOAA’s HYSPLIT atmospheric transport and dispersion modeling system. Bull. Am. Meteorol. Soc. 96, 2059–2077. https://doi.org/10.1175/BAMS-D-14-00110.1.

Timonen, H., Cubison, M., Aurela, M., Brus, D., Lihavainen, H., Hillamo, R., Canagaratna, M., Nekat, B., Weller, R., Worsnop, D., Saarikoski, S., 2016. Applications and limitations of constrained high-resolution peak fitting on low resolving power mass spectra from the ToF-ACSM. Atmos. Meas. Tech. 9, 3263–3281. https://doi.org/10.5194/amt-9-3263-2016.

Tkacik, D.S., Lambe, A.T., Jathar, S., Li, X., Presto, A.A., Zhao, Y., Blake, D., Meinardi, S., Jayne, J.T., Croteau, P.L., Robinson, A.L., 2014. Secondary organic aerosol formation from in-use motor vehicle emissions using a potential aerosol mass reactor. Environ. Sci. Technol. 48, 11235–11242. https://doi.org/10.1021/es502239v.

Tobler, A.K., Skiba, A., Canonaco, F., Močnik, G., Rai, P., Chen, G., Bartyzel, J., Zimnoch, M., Styszko, K., Nęcki, J., Furger, M., Różański, K., Baltensperger, U., Slowik, J.G., Prevot, A.S.H., 2021. Characterization of non-refractory (NR) PM1 and source apportionment of organic aerosol in Kraków, Poland. Atmos. Chem. Phys. 21, 14893–14906. https://doi.org/10.5194/acp-21-14893-2021.

Ulbrich, I.M., Canagaratna, M.R., Zhang, Q., Worsnop, D.R., Jimenez, J.L., 2009. Interpretation of organic components from Positive Matrix Factorization of aerosol mass spectrometric data. Atmos. Chem. Phys. 28.

van der A, R.J., Eskes, H.J., Boersma, K.F., van Noije, T.P.C., Van Roozendael, M., De Smedt, I., Peters, D.H.M.U., Meijer, E.W., 2008. Trends, seasonal variability and dominant NOx source derived from a ten year record of NO2 measured from space. J. Geophys. Res. 113, D04302 https://doi.org/10.1029/2007JD009021.

Via, M., Minguillón, M.C., Reche, C., Querol, X., Alastuey, A., 2021. Increase in secondary organic aerosol in an urban environment. Atmos. Chem. Phys. 21, 8323–8339. https://doi.org/10.5194/acp-21-8323-2021.

Vlachou, A., Daellenbach, K.R., Bozzetti, C., Chazeau, B., Salazar, G.A., Szidat, S., Jaffrezo, J.-L., Hueglin, C., Baltensperger, U., Haddad, I.E., Prévôt, A.S.H., 2018. Advanced source apportionment of carbonaceous aerosols by coupling offline AMS and radiocarbon size-segregated measurements over a nearly 2-year period. Atmos. Chem. Phys. 18, 6187–6206. https://doi.org/10.5194/acp-18-6187-2018.

Vlachou, A., Tobler, A., Lamkaddam, H., Canonaco, F., Daellenbach, K.R., Jaffrezo, J.-L., Minguillón, M.C., Maasikmets, M., Teinemaa, E., Baltensperger, U., El Haddad, I., Prévôt, A.S.H., 2019. Development of a versatile source apportionment analysis based on positive matrix factorization: a case study of the seasonal variation of organic aerosol sources in Estonia. Atmos. Chem. Phys. 19, 7279–7295. https://doi.org/10.5194/acp-19-7279-2019.

Xu, L., Suresh, S., Guo, H., Weber, R.J., Ng, N.L., 2015. Aerosol characterization over the southeastern United States using high-resolution aerosol mass spectrometry: spatial and seasonal variation of aerosol composition and sources with a focus on organic nitrates. Atmos. Chem. Phys. 15, 7307–7336. https://doi.org/10.5194/acp-15-7307-2015.

Young, D.E., Allan, J.D., Williams, P.I., Green, D.C., Flynn, M.J., Harrison, R.M., Yin, J., Gallagher, M.W., Coe, H., 2015. Investigating the annual behaviour of submicron secondary inorganic and organic aerosols in London. Atmos. Chem. Phys. 15, 6351–6366. https://doi.org/10.5194/acp-15-6351-2015.

Zhang, Q., Jimenez, J.L., Canagaratna, M.R., Ulbrich, I.M., Ng, N.L., Worsnop, D.R., Sun, Y., 2011. Understanding atmospheric organic aerosols via factor analysis of aerosol mass spectrometry: a review. Anal. Bioanal. Chem. 401, 3045–3067. https://doi.org/10.1007/s00216-011-5355-y.

Zhang, Y., Favez, O., Petit, J.-E., Canonaco, F., Truong, F., Bonnaire, N., Crenn, V., Amodeo, T., Prévôt, A.S.H., Sciare, J., Gros, V., Albinet, A., 2019. Six-year source apportionment of submicron organic aerosols from near-continuous highly time-resolved measurements at SIRTA (Paris area, France). Atmos. Chem. Phys. 19, 14755–14776. https://doi.org/10.5194/acp-19-14755-2019.

Zotter, P., Herich, H., Gysel, M., El-Haddad, I., Zhang, Y., Močnik, G., Hüglin, C., Baltensperger, U., Szidat, S., Prévôt, A.S.H., 2017. Evaluation of the absorption Ångström exponents for traffic and wood burning in the Aethalometer-based source apportionment using radiocarbon measurements of ambient aerosol. Atmos. Chem. Phys. 17, 4229–4249. https://doi.org/10.5194/acp-17-4229-2017.